A Multi-Parametric Composite Approach for the Optimization of Wind Turbine Blades using Double-Double Laminates

Edgar Werthen[1], Gustavo Nunes Ribeiro[1], Sascha Dähne[1], David Zerbst[1], Lennart Tönjes[1], and Christian Hühne[1]

[1]DLR German Aerospace Center, Institute of Lightweight Systems, Lilienthalplatz 7, 38108 Braunschweig, Germany

Correspondence: Edgar Werthen (edgar.werthen@dlr.de)

Abstract. As wind turbines scale to meet growing energy demands, blade structures face increasingly demanding performance requirements. This work addresses this challenge by extending the design space of composite blades through the substitution of traditional triaxial laminates with Double-Double (DD) laminates. While triaxial laminates are widely used due to their convenient layup and manufacturability, they are rarely scrutinized in literature and often lead to suboptimal structural performance. To enable this substitution, a multi-parametric composite modeling approach is developed and integrated into a gradient-based optimization framework. This architecture enables the coexistence of discrete and continuous laminate formulations within a single panel, allowing for detailed, skin-wise optimization of sandwich structures. The approach is applied to a modified blade design of the IEA-15-240 Reference Wind Turbine. Results demonstrate that DD laminates provide a more effective buckling-oriented design, resulting in significant mass savings in the shell structure.

1 Introduction

As wind turbines evolve to support greater energy supply, scaling rotor size has become essential to maximizing power output. The annual energy production (AEP) increases proportionally to the square of the blade radius (Gasch and Twele, 2012), whereas blade mass scales to the power of around 2.4 with the blade radius (Rosemeier and Krimmer, 2022). This imbalance creates a structural challenge: increasing blade length raises the aerodynamic potential, but also increases mass and loads.

Composite materials have been fundamental in counteracting these trends. Beyond a high strength-to-weight ratio, their mechanical response can be tailored to the dominant load paths through ply orientation and stacking sequence. Unlike isotropic metallic alloys, fiber-reinforced laminates enable control of directional stiffness and coupling, improving structural efficiency. As a result, modern blades rely predominantly on composites, which account for approximately 93% of their structural weight (Liu and Barlow, 2017).

Although reinforced plastics offer significant potential for weight reduction, they also introduce challenges in design, analysis, optimization, and manufacture. Beyond selecting the fiber composition and matrix material, the layup configuration must be defined, including ply angles, stacking order, and thickness distributions. In practice, blades are often designed using generic laminate families with pre-established angles and thicknesses, which are then treated as homogenized transversely isotropic single layers for design and analysis. Their widespread adoption is also motivated by manufacturability, because complex

25 layups significantly increase cost, defect sensitivity, and tapering effort. Standardized families, particularly when produced with fabrics, reduce variability and simplify both production and structural modeling.

Aligned with industry trends and the demand for a new baseline in the 10–20 MW range, the IEA Wind TCP Task 37 introduced the IEA 15 MW RWT in March 2020—an offshore turbine intended to push the state of the art (Gaertner et al., 2020). To accommodate higher power capture, the blade length and mass were scaled to 117 m and 65 t, respectively. Structurally,

30 the design follows a traditional layout with two main spars and spar caps, complemented by shear webs that extend from 10% to 95% of the blade span. The triaxial glass laminate covers most of the structure, while the shear webs are reinforced with biaxial glass fibers. The internal volume, apart from key load-bearing components, is filled with medium-density foam in a sandwich configuration to limit weight. The trailing and leading edges feature a uniaxial glass laminate, while the spar caps employ uniaxial carbon laminate as the core material. The structural concept is shown in Figure 1.
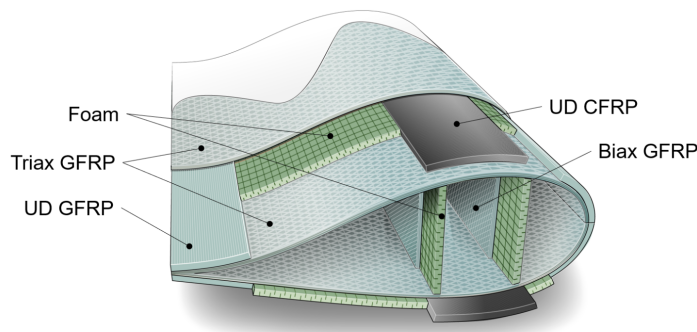
Figure 1. IEA 15 MW structural concept. Source: (Werthen et al., 2023).

35 Beyond the specific architecture of the IEA 15 MW, the selection of laminate materials reflects a consistent trend across successive reference models—dominated by triaxial laminate applications. Early designs, such as the NREL 1.5 MW, 3 MW, and 5 MW reference wind turbines (Rinker and Dykes, 2018), extensively employed triaxial glass laminates, wrapping both the shell and spar webs. More recent baselines, including the DTU 10 MW (Bak et al., 2013), IEA 10 MW (Bortolotti et al., 2019), IEA 15 MW (Gaertner et al., 2020), and IEA 22 MW (Zahle et al., 2024), retain triaxial laminates primarily on the shell,

40 while the spar webs employ biaxial laminates. Despite this evolution, triaxial materials still represent a substantial share of the overall blade mass.

A typical triaxial layup follows the sequence $[-45°/0°/+45°]$, comprising roughly 50% unidirectional (0°) and 50% off-axis (±45°) plies (Camarena et al., 2022). This configuration is attractive for its balanced response under general loading, providing in-plane shear resistance, bending stiffness, and improved buckling performance (Castro, 2018). However, its near-

45 generic character limits the tailoring of stiffness and directional coupling. For this reason, triaxial laminates are often adopted in less optimized industrial contexts due to their simplicity and generality (Samborsky and Mandell, 1996).

Building on the reference models, several studies explored blade optimization under different design settings. Sjølund and Lund (2018) optimized only the thickness of a variety of layers on a 73.5 m blade and achieved a 19.4% mass reduction. Serafeim et al. (2022) tailored spar-cap stiffness by rotating the UD fibers, obtaining a $5.8°$ off-axis solution and an 8.3%

50   reduction on the DTU 10 MW blade. Hayat et al. (2022) conducted material and thickness optimization of the spar caps (glass, hybrid, carbon), reporting a reduction of up to 26.4%, consistent with the spanwise strategy adopted in the IEA 15 MW baseline. Scott et al. (2022) optimized the IEA 15 MW using thickness laws, material mix, and spar-cap position; however, under frozen loads, they required a 34.7% mass increase to recover stability. Extending stiffness tailoring, Couto et al. (2023) used region-wise laminate optimization with discrete angle sets but remained constrained by the limited orientations.

55   The vast, discrete design space of composite laminates intrinsically motivates simplifications in their description and design. Most commonly, ply orientations are fixed, and only thickness is scaled (e.g., (Sjølund and Lund, 2018; Hayat et al., 2022; Scott et al., 2022)); in other cases, the space is restricted to a small discrete set of angles, reducing tailoring margin (e.g., (Couto et al., 2023)). A similar pattern appears in aeronautics, where quad-laminates—an extension of triax with an added $90°$ ply—are widely used; they deliver behavior closer to metallic alloys but at the cost of a more complex design and optimization

60   pipeline (Tsai, 2021).

To address these limitations, Tsai (2021) introduced the Double–Double (DD) laminate class. A DD is defined by two angles (Φ, Ψ) forming the four-ply building block $[\pm\Phi, \pm\Psi]_r$ repeated r times. This yields a continuous, balanced parameterization with straightforward homogenization, making design and optimization less complex. A key advantage is tapering: building blocks can be dropped to transition between neighboring panels without symmetry constraints (Kappel et al., 2024). From a

65   manufacturing standpoint, Kappel and Tsai (2024) demonstrated DD laminates using prepreg and vacuum infusion, predominantly prepreg with off-the-shelf materials, which is consistent with processes also used in wind turbine blade production (Mishnaevsky et al., 2017).

Almeida et al. (2025) surveyed the use of Double–Double laminates across applications and discussed their implications. Notably, Garofano et al. (2023) compared DD laminates with conventional layups in fuselage structures and reported a 34%

70   weight reduction. Given the structural parallels between wings and blades—slender, tapered panels under complex loading, Kappel (2022) applied DD laminates to aircraft wing panels and demonstrated about 8% weight savings relative to an already optimized metallic panel. Moreover, Zerbst et al. (2025) integrated a Double–Double plate formulation into a gradient-based optimization environment for composite structures called *lightworks* (Dähne et al., 2024) and validated it on a wing-box case. These results highlight the weight-saving potential of Double–Double laminates across aerospace structures and their initial

75   integration into *lightworks*.

Extending this capability to wind-turbine blades requires higher modeling fidelity, as blade panels are typically sandwich structures composed of multiple materials through the thickness. In practice, outer face sheets may follow a continuous Double–Double description, whereas cores remain discrete laminates. Representing such combinations requires a clear parameterization strategy, in which each constituent material defines its own design variables, while consistently contributing to the

80   overall panel response. To support this requirement, a modular and multi-parametric plate formulation is introduced. It allows for the independent parameterization of sub-components and their integration into a unified structural layer. This approach

accommodates both continuous and discrete laminates within the same stack, and enables the replacement of conventional triaxial skins with Double–Double laminates. This way, expanding the design space towards more adaptable stiffness behavior.

1.1 Objectives

85 In light of the above, the central objective of this study is to enable structural mass optimization in large wind turbine blades by expanding the design space of sandwich composite panels. This is achieved by introducing Double–Double laminates in place of the predefined stiffness-fixed triaxial laminates.

To make this substitution viable within sandwich panels, a multi-parametric composite approach is introduced and implemented in the *lightworks* optimization environment. The approach models sandwich structures as modular assemblies of 90 independently parameterized sub-composites, enabling materials with different structural foundations, such as layer-based and continuous formulations, to coexist across the panel thickness.

This work naturally follows as a continuation of the study by Werthen et al. (2023), who employed *lightworks* for large-scale blade optimization using a simplified sandwich representation, in which each component (e.g., a triaxial laminate) was modeled as a single equivalent layer in the stack. In contrast, the present approach expands the formulation to incorporate 95 Double–Double laminates, which is demonstrated on the CRC-15-240 blade, an in-house modified version of the IEA-15-240 reference wind turbine. This constitutes the first application of Double–Double laminates in wind turbine blade design and represents a step forward in advancing composite optimization for the wind industry.

1.2 Structure of the paper

The development of this work is organized into three consecutive phases, each addressing a distinct layer of the proposed 100 methodology. All implementations are subjected to verification and testing, with feedback loops guiding refinements at each stage.

The first phase focuses on Double–Double laminates as replacements for the triax. It includes reviewing the mechanical role and limitations of triaxial laminates, characterizing the stiffness and failure behavior of Double–Double configurations, performing parametric load studies, and implementing a restricted "hard" variant with fixed $\Phi = 0°$ for intermediate optimization 105 tests.

The second phase extends the *lightworks* structural model to support multi-parametric composites. This involves developing a class to handle modular stacking, implementing algorithms for stiffness assembly and load distribution through the thickness, and integrating the formulation into the structural and optimization pipeline.

The third phase applies the methodology to the CRC-15-240 blade, demonstrating the practical use of the multi-parametric 110 framework and Double–Double laminates in large-scale optimization. This involves adapting auxiliary tools to the framework and analyzing outcomes in terms of mass reduction, design-space expansion, and material property distribution along the span.

The subsequent sections of this study are organized as follows. Section 2 investigates Double–Double laminates in comparison to triaxial laminates. Section 3 introduces the multi-parametric approach and demonstrates it through a single-panel case.

Section 4 applies the methodology to the CRC-15-240 blade, detailing the optimization setup. Section 5 presents a comparative
115   assessment of results. Finally, Section 6 summarizes the key findings.

2   Characterization of Double-Double and Triaxial Laminates

The Double-Double laminate concept, introduced by Tsai (2021), represents a significant advancement in the efficient design
of composite structures. Based entirely on the Classical Laminate Theory (CLT), its formulation requires no additional as-
sumptions and, notably, removes the need for mid-plane symmetry, traditionally imposed to avoid bending-extension coupling,
120   simplifying design and manufacturing constraints.

A typical DD laminate is composed of repeated building blocks (BBs), each containing four plies arranged in two balanced
angle pairs. Among the possible stacking options, the configuration $[\Phi/-\Psi/-\Phi/\Psi]$ has been shown to yield superior ho-
mogenization characteristics (Tsai, 2021), and is therefore adopted throughout this work. The complete laminate is formed by
repeating this block r times through the thickness, resulting in the configuration $[\pm\Psi/\pm\Phi]_{rT}$, where the subscript T denotes
125   the total stack, following the Nettles convention (Nettles, 1994).

2.1   Homogenization

The main advantage of DD laminates lies in their potential for homogenization: as the number of building blocks increases,
the bending and extensional stiffness matrices ($[\mathbf{D}]$ and $[\mathbf{A}]$) approach proportionality, while the coupling matrix ($[\mathbf{B}]$) tends
toward zero. The resulting structure exhibits a layer-position-independent response with minimal coupling between in-plane
130   and out-of-plane behaviors.

As reported in Zerbst et al. (2025), the normalized matrices exhibit characteristic dependencies on r. These trends indicate
that with increasing r, the off-diagonal terms of $[\mathbf{B}^*]$ decay as $1/r$, while specific coupling terms in $[\mathbf{D}^*]$ vanish at a rate of
$1/r^2$. To formalize this, Tsai (2021) elaborated two conditions to be met for assumed homogenization:

$$\forall i,j \in \{1,2,6\}: \quad \left|A_{ij}^* - D_{ij}^*\right|, \left|B_{ij}^*\right| < \alpha \cdot \text{TSAI} \tag{1}$$

135   where α is a prescribed fraction of the Tsai modulus, defined as the trace of the ply stiffness matrix ($\text{TSAI} = \text{Tr}[Q]$). Acting
as a threshold to define acceptable levels of coupling and stiffness mismatch, Tsai (2021) recommends $\alpha = 0.02$.

Once these conditions are met, the laminate behavior can be approximated using only the extensional stiffness matrix $[\mathbf{A}]$,
and the bending stiffness $[\mathbf{D}]$ can be derived as:

$$[\mathbf{A}] = \sum_{k=1}^{4}\left([\bar{\mathbf{Q}}]_k \frac{t_{\text{lam}}}{4}\right), \quad [\mathbf{B}] = \mathbf{0}, \quad [\mathbf{D}] = \frac{t_{\text{lam}}^2}{12}[\mathbf{A}], \tag{2}$$

140   where $[\bar{\mathbf{Q}}]_k$ denotes the transformed reduced stiffness matrix of the k-th ply in the building block, dependent on $\pm\Phi$ or $\pm\Psi$.

2.2 Design Space

According to Tsai and Melo (2015a), any laminate can be described through lamination parameters: a continuous stiffness representation grounded in invariant theory. To characterize the design space of Double-Double laminates relative to conventional triaxial configurations, their formulation is briefly recalled.

The general formulation of the lamination parameters can be expressed as follows, in accordance with Zerbst et al. (2025):

$$V_x^A = \frac{1}{t_{\text{lam}}} \sum_{k=1}^{N} (z_k - z_{k-1}) W_x, \tag{3}$$

$$V_x^B = \frac{1}{t_{\text{lam}}^2} \sum_{k=1}^{N} (z_k^2 - z_{k-1}^2) W_x, \tag{4}$$

$$V_x^D = \frac{4}{t_{\text{lam}}^3} \sum_{k=1}^{N} (z_k^3 - z_{k-1}^3) W_x, \tag{5}$$

where z_k is the distance from the k-th ply to the laminate mid-plane, and W_x are trigonometric functions of the ply angle θ_k:

$$W_x = \begin{cases} \cos(2\theta_k), & x = 1, \\ \sin(2\theta_k), & x = 2, \\ \cos(4\theta_k), & x = 3, \\ \sin(4\theta_k), & x = 4. \end{cases} \tag{6}$$

For a homogenized DD laminate, this formulation simplifies considerably. All coupling-related lamination parameters $V_{1,2,3,4}^B$ vanish, and due to the proportional nature of $[\mathbf{A}]$ and $[\mathbf{D}]$, the bending parameters equal the extensional ones ($V_x^A = V_x^D$). The resulting formulation thus reduces to four unique values, among which only V_1^A and V_2^A (and their bending counterparts) vary with the fiber angles Φ and Ψ:

$$V_1^A = \tfrac{1}{2}[\cos(2\Phi) + \cos(2\Psi)] = V_1^D, \tag{7}$$

$$V_2^A = \tfrac{1}{2}[\cos(4\Phi) + \cos(4\Psi)] = V_2^D, \tag{8}$$

$$V_3^A = 0 = V_3^D, \quad V_4^A = 0 = V_4^D, \quad V_{1,2,3,4}^B = 0. \tag{9}$$

Thus, the entire design space of a DD laminate can be visualized in the V_1^A–V_2^A plane, where each admissible combination of the angle pair $\{\Phi, \Psi\}$ maps to a specific point. Figure 2 illustrates the full DD design space, as mathematically described in Zhao et al. (2023).

An important aspect to highlight is the role of the lamination parameter V_2^A. Laminates with $V_2^A \geq 0$ are classified as hard laminates due to their greater resistance to normal stresses, whereas those with $V_2^A < 0$ are called soft laminates, exhibiting improved shear and buckling performance.

A typical triaxial laminate can be interpreted as a particular case of the Double-Double configuration, though with a stacking arrangement $[\pm 0 / \pm 45]$ that is not optimal for homogenization (Tsai, 2021). Owing to its position along the vertical axis of the
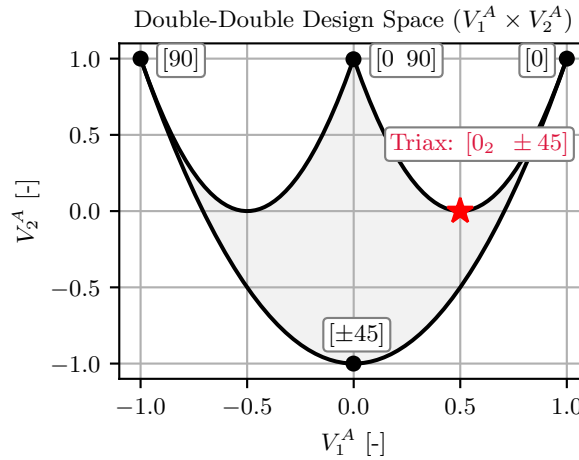
Figure 2. Design space of DD laminates in the V_1^A–V_2^A plane.

design space, the triaxial laminate lies within the hard region. Nevertheless, the inclusion of $\pm45°$ plies determines a hybrid character, improving its shear and buckling resistance. Despite their practicality, triaxial laminates are ill-suited to optimization: they are fixed at a single point in the lamination-parameter space, enforcing a predefined normal–shear compromise. As a result, their capacity to adapt to specific load cases is limited, unless the optimal solution coincidentally aligns with the same fiber orientations.

2.3 Strength Criterion

For discrete laminates, strength evaluations are typically performed at the ply level (i.e., Tsai-wu criterion). However, when employing a continuous homogenized formulation, ply-level evaluation becomes inconsistent with the design representation. In this context, a laminate-level failure criterion is essential to maintain continuous formulation without layup reconstruction.

One laminate-level alternative is the strain-based omni-envelope criterion proposed by Tsai and Melo (2015b). This method is derived from the classical quadratic failure criterion in stress space and reformulated in strain space. The general form of the failure condition is expressed as:

$$H_{ij}\varepsilon_i\varepsilon_j + H_i\varepsilon_i = 1 \tag{10}$$

where H_{ij} and H_i are material-dependent coefficients derived from strain invariants. These coefficients depend on the stiffness matrix and ply orientation, and their derivation is detailed in Kappel (2023).

The omni-envelope extends the ply-level criterion by superimposing the strain-space envelopes of unidirectional plies across all fiber orientations present in the laminate, following the Tsai-wu criterion (Kappel, 2022). The result is a global strain envelope that represents the union of all individual failure surfaces. Zerbst et al. (2025) discusses its use for double-double laminates using *lightworks*.

2.4 Design Space Exploration under In-Plane Loads

Under distinct loading conditions, double-double laminates adjust their angles to optimize the response in relation to a specific objective (e.g., mass), exploring the full design space capacity previously shown in Figure 2. This analysis considers only strength constraints, provided by the omni-envelope criterion, and disregards any stability assessment. The focus remains exclusively on material-level response.

The exploration includes pure and combined loading conditions involving uniaxial and shear loads: a scenario similar to the wind turbine blade application explored in this study. The load cases are summarized in Table 1.

Table 1. In-plane load combinations used for design space exploration.

Case #	Name	n_x [N m^{-1}]	n_{xy} [N m^{-1}]
1	UD Tension	$+1.0 \times 10^6$	0
2	UD Compression	-1.0×10^6	0
3	Pure Shear	0	2.0×10^5
4	Tension + Shear	$+1.0 \times 10^6$	5.0×10^5
5	Compression + Shear	-1.0×10^6	5.0×10^5

Under axial tension and compression (Cases #1 and #2), the optimized DD laminate aligns both fiber angles with the load direction, defined here as $\Phi = \Psi = 0°$, since the fibers act as the primary load carriers. Figure 3 illustrates the resulting mass distribution across different angle combinations: while the DD laminate converges to the optimal alignment, the triaxial configuration remains fixed, with one angle aligned with the load and the other offset by $45°$, resulting in a mass increase. The compressive case exhibits nearly identical behavior, differing only in allowable limits due to the material's higher tensile strength.

When subjected to pure shear (Case #3), the optimal stacking shifts toward intermediate angles, with $45°$ emerging as the dominant orientation, as shown in Figure 4. This response reflects classical shear mechanics, where maximum shear stress is resolved along $\theta = 45°$ planes, producing a corner-driven deformation mode that is best resisted by fibers oriented in those directions. Once more, the triax shows mass increase due to additional non-optimized $0°$ plies.

In the tension–shear case (Case 4#), shown in Figure 5, the optimal fiber angles shift toward lower values, corresponding to the hard-laminate region. The solution remains offset from the $(0,0)$ coordinate, with both Φ and Ψ lying between $0°$ and $45°$. This trend is consistent with the pure tension and pure shear responses previously observed in Figure 3 and Figure 4.

Conversely, the compression–shear interaction (Case 5#), illustrated in Figure 6, produces a markedly different result. The optimized angles shift toward higher values, which increases the off-axis orientation and, as a consequence, generates larger transverse normal stress σ_2.

This behavior follows directly from the Tsai–Wu interaction terms, shown in Figure 7: the shear strength is coupled with the transverse normal stress, such that moderate compression in the 2-direction increases the effective shear strength. Physically,
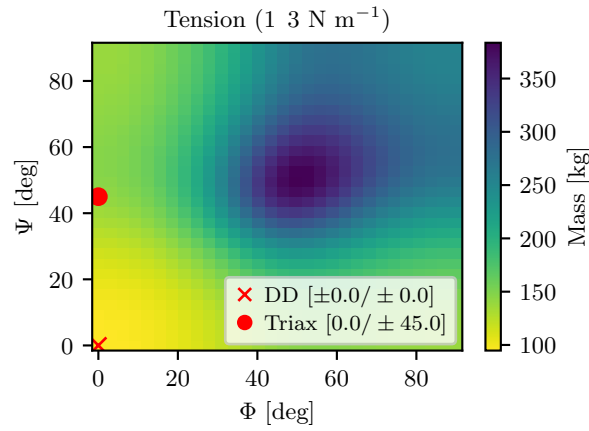
Figure 3. Optimized mass distribution for the DD laminate under axial tension.
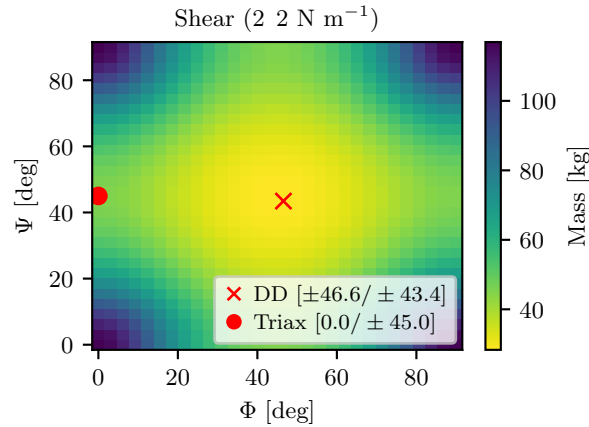
Figure 4. Optimized mass distribution for the DD laminate under pure shear loading.

210 this corresponds to the fibers being laterally constrained by the matrix, which delays shear-driven failure. However, once σ_2 becomes sufficiently large, the quadratic compression term dominates, and the allowable shear strength drops again. This mechanism explains why the proportion n_x/n_{xy} is critical for determining the optimal angle shift in this case.

These results underscore that stiffness-based tailoring, even in its simplified form, captures design freedoms that are unexplored by triaxial laminates, whose fixed fiber arrangement constrains their ability to adapt to varying loads.
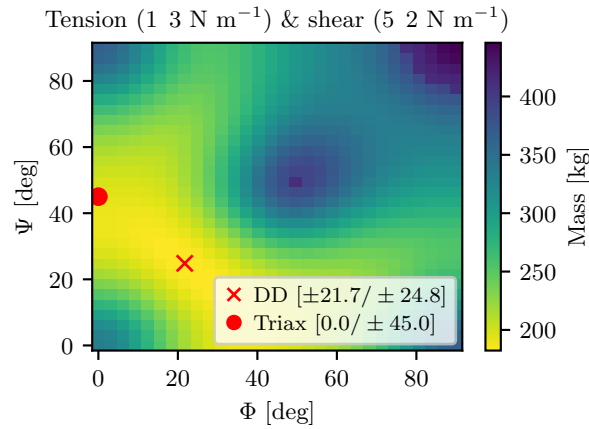
Figure 5. Optimized mass distribution for the DD laminate under combined tension and shear loading.
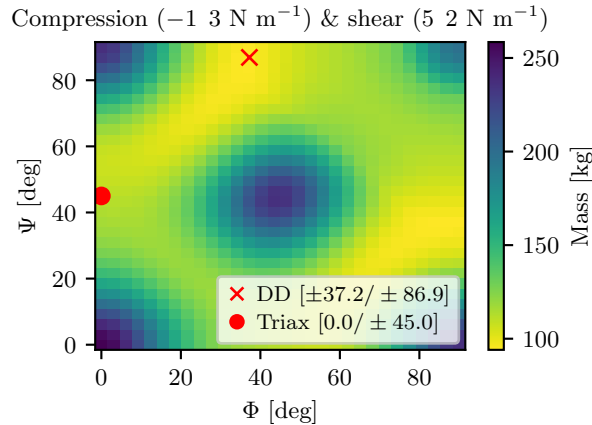
Figure 6. Optimized mass distribution for the DD laminate under combined compression and shear loading.

3 Multi-Parametric Composites

Conventional structural models in structural optimization, such as those used in previous large-blade studies, describe each panel through a set of homogenized layers (e.g. Sjølund and Lund (2018); Hayat et al. (2022); Scott et al. (2022); Werthen et al. (2023)). While efficient, this approach simplifies the internal composition of sandwich structures into equivalent layers within a laminate, typically limited to three homogenized materials.

The multi-parametric formulation introduces a modular description of composite panels (Figure 8). Each panel is decomposed into a stack of independently parameterized sub-composites, each retaining its own material model and design variables. This structure allows, for example, Double–Double laminates to coexist with unidirectional or foam components within the
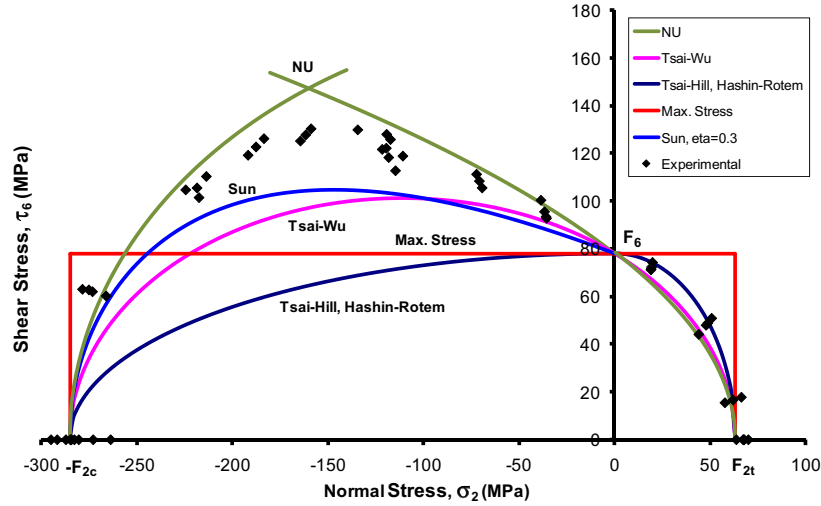
Figure 7. Tsai–Wu τ_{12}–σ_2 failure envelope. Source: Daniel et al. (2011).

same stack. Design variables are defined at the composite level, enabling independent control of each sub-component's parameters, such as fiber angles and thickness, without constraining them to a single, homogenized behavior. Whereas conventional

225 models assemble stiffness from individual laminate layers, the new approach computes and superposes the stiffness of each composite sub-component, maintaining analytical consistency while expanding the design space available for optimization.

3.1 Stiffness Superposition

To enable a generalized treatment of stiffness for any combination of composite formulations, the stack must be interpreted as a sequence of materials, each characterized solely by its stiffness matrix, thickness, and position across the panel's thickness. This

230 abstraction enables the creation of a global stiffness matrix $[\mathbf{ABD}]_{\text{global}}$ from various combinations of materials, regardless of whether the underlying model is discrete or continuous. As long as each material supplies its individual stiffness matrix $[\mathbf{ABD}]_{\text{local}}$ and total thickness, the modular integration remains intact.

The core principle enabling stiffness superposition is the analytical shift of the reference plane for each component, from its original mid-plane, as defined in Classical Laminate Theory, to a common reference shared across all material blocks. This

235 alignment allows for the consistent transformation of stiffness contributions, enabling their direct summation into a global stiffness matrix. The entire process is fully grounded in the CLT without introducing any additional assumptions.

Figure 9 illustrates the concept of an arbitrary reference plane shift for a single laminate.

For such a shift, the position of any point along the thickness can be expressed as:

$$z^{new} = z^0 + \Delta z, \tag{11}$$

240 where z^0 is the coordinate with respect to the original reference plane, Δz is the signed offset between the planes, and z^{new} is the transformed coordinate relative to the new reference.
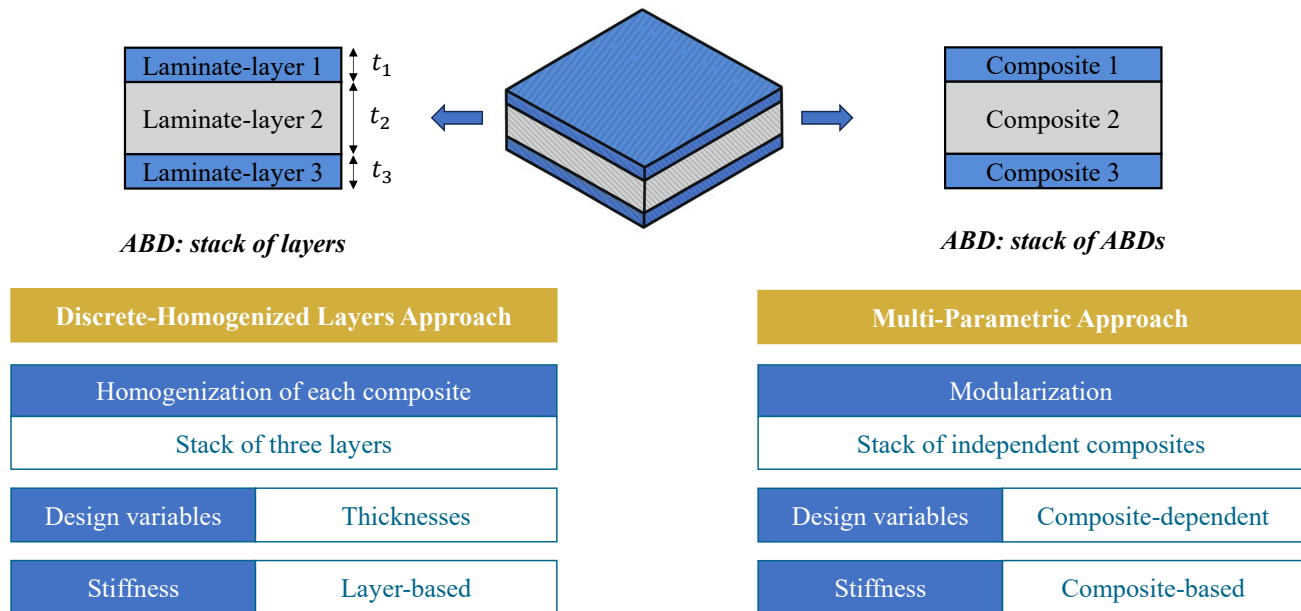
Figure 8. Conceptual comparison between the discrete–homogenized and multi-parametric formulations.
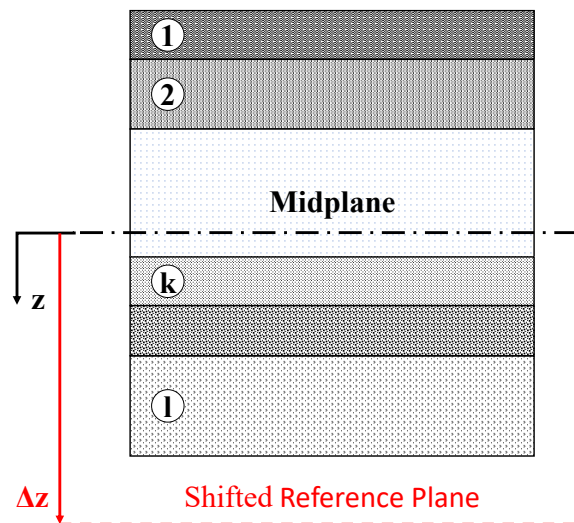
Figure 9. Plane shift from the original mid-plane.

Using this definition, the transformed stiffness matrices $[\mathbf{A}^{new}]$, $[\mathbf{B}^{new}]$, and $[\mathbf{D}^{new}]$ can be defined as:

$$[\mathbf{A}^{new}] = \sum_k [\bar{\mathbf{Q}}_k]\left[z_{k-1}^{new} - z_k^{new}\right], \tag{12}$$

245

$$[\mathbf{B}^{new}] = -\frac{1}{2}\sum_k [\bar{\mathbf{Q}}_k]\left[\left(z_{k-1}^{new}\right)^2 - \left(z_k^{new}\right)^2\right], \tag{13}$$

$$[\mathbf{D}^{new}] = \frac{1}{3}\sum_k [\bar{\mathbf{Q}}_k]\left[\left(z_{k-1}^{new}\right)^3 - \left(z_k^{new}\right)^3\right]. \tag{14}$$

By substituting Equation 11 into Equations 12, 13 and 14, and expanding each term, the transformed stiffness matrices can be written as functions of the original matrices (^{0}) and the shift Δz. The resulting transformations are shown below, while their

250   derivations are provided in Appendix A:

$$\boxed{\begin{aligned}
[\mathbf{A}^{\text{new}}] &= [\mathbf{A}^0], \\
[\mathbf{B}^{\text{new}}] &= [\mathbf{B}^0] + \Delta z\,[\mathbf{A}^0], \\
[\mathbf{D}^{\text{new}}] &= [\mathbf{D}^0] + 2\Delta z\,[\mathbf{B}^0] + \Delta z^2\,[\mathbf{A}^0].
\end{aligned}} \tag{15}$$

Once the $[\mathbf{ABD}]$ formulation is derived with respect to an arbitrary reference plane, the superposition of multiple composites can be consistently established. Figure 10 illustrates a generic stack composed of multiple material blocks, each contributing to the overall stiffness, given the plane shift to a common one.

255   Although the reference plane could, in theory, be positioned arbitrarily along the z-axis, it is imposed to coincide with the mid-plane of the whole stack. This aligns the computed stiffness terms with the plate formulation, where loads and deformations are defined relative to the mid-plane. The resulting superposition formulation is given in Equations 16, 17 and 18.

$$[\mathbf{A}] = \sum_k [\mathbf{A}_k^0] \tag{16}$$

$$[\mathbf{B}] = \sum_k \left([\mathbf{B}_k^0] + \Delta z_k\,[\mathbf{A}_k^0]\right) \tag{17}$$

260

$$[\mathbf{D}] = \sum_k \left([\mathbf{D}_k^0] + 2\Delta z_k\,[\mathbf{B}_k^0] + \Delta z_k^2\,[\mathbf{A}_k^0]\right) \tag{18}$$
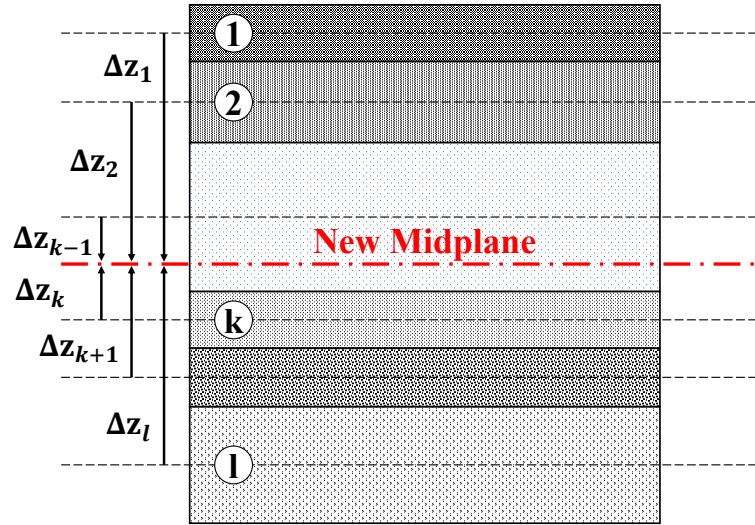
Figure 10. Superposition of different composite blocks.

3.2 Load Distribution

In the context of structural assessment, stability and strength evaluations operate at distinct hierarchical levels. Stability is assessed at the panel level, based on the global geometry, stiffness matrix, and applied loads. Once the governing criterion is defined, the procedure follows a fixed analytical pipeline dependent solely on these macroscopic parameters. Strength eval-

265 uation, in contrast, is performed at the material level to capture the behavior of each constituent composite. This requires distributing the global load state across the individual components of the stack so that each sub-composite is assessed independently according to its local strain field and failure criterion.

From the solver, each panel receives a set of membrane forces ($\mathbf{N}$) and bending moments ($\mathbf{M}$), which serve as the input loads for subsequent evaluations. For strength assessment, these loads are converted into strain quantities using the plate stiffness

270 relation shown in Equation 19, obtained through inversion of the $[\mathbf{ABD}]$ matrix. This operation yields the mid-plane strain ε^0 and curvature κ for the panel.

$$\begin{Bmatrix} \varepsilon^0 \\ \kappa \end{Bmatrix} = \begin{bmatrix} [\mathbf{A}] & [\mathbf{B}] \\ [\mathbf{B}] & [\mathbf{D}] \end{bmatrix}^{-1} \begin{Bmatrix} \mathbf{N} \\ \mathbf{M} \end{Bmatrix}. \tag{19}$$

As defined in Equation 20, the strain at any point through the thickness of a laminate is represented as a superposition of membrane strain and bending-induced curvature:

$$275 \quad \begin{Bmatrix} \varepsilon_x \\ \varepsilon_y \\ \gamma_{xy} \end{Bmatrix} = \begin{Bmatrix} \varepsilon_x^0 \\ \varepsilon_y^0 \\ \gamma_{xy}^0 \end{Bmatrix} + z \begin{Bmatrix} \kappa_x \\ \kappa_y \\ \kappa_{xy} \end{Bmatrix}. \tag{20}$$

When curvature is non-zero, the resulting strain varies linearly through the laminate thickness for each strain component. This behavior is illustrated in Figure 11.
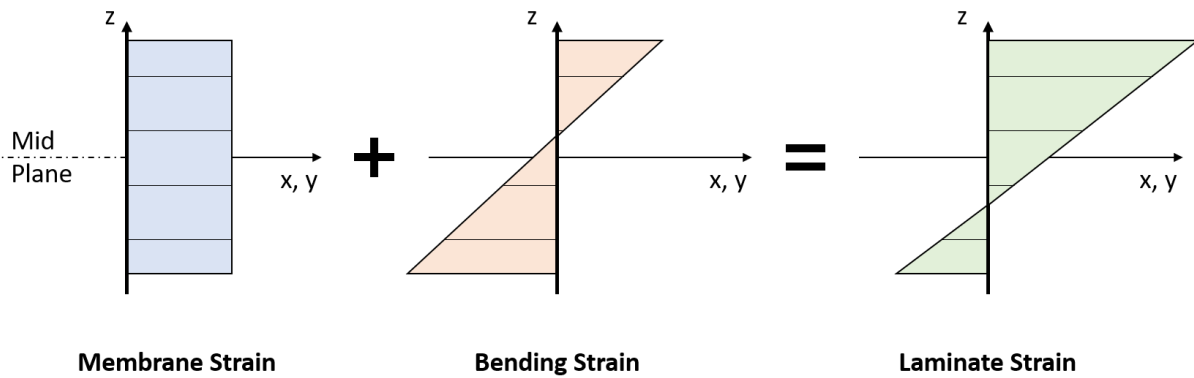
Figure 11. Resultant strain for a laminate under membrane and bending loads.

In a multi-composite stack, the same principle of linear strain distribution applies. However, to preserve the modularity of the multi-parametric composites formulation, each composite must be evaluated independently with respect to its position within
280   the stack.

This is achieved by mapping the global deformation state, defined by the mid-plane strain and curvature of the entire laminate, into a local strain state for each individual skin. Specifically, a relative mid-plane strain is computed for each skin, accounting for the contribution of curvature based on the vertical offset between the global mid-plane and the mid-plane of the corresponding sub-skin.

285   Mathematically, the local mid-plane strain for each sub-skin is given by:

$$\varepsilon_{\text{sub-skin}}^0 = \varepsilon_{\text{global}}^0 + \Delta z \cdot \boldsymbol{\kappa} \tag{21}$$

where Δz denotes the signed distance between the mid-plane of the sub-skin and the global mid-plane of the stack.

Consequently, the strain distribution within each sub-skin can be expressed as:

$$\varepsilon_{\text{sub-skin}}(z) = \varepsilon_{\text{sub-skin}}^0 + \boldsymbol{\kappa} \cdot z, \quad z \in \left[-\frac{t_{\text{sub-skin}}}{2}, \frac{t_{\text{sub-skin}}}{2} \right]. \tag{22}$$

290   This piecewise formulation results in a segmented strain profile across the laminate thickness, with each segment corresponding to a distinct material block. Importantly, it ensures that each skin is evaluated using its own local reference and geometry, entirely decoupled from the global assembly. An example of this concept is illustrated in Figure 12
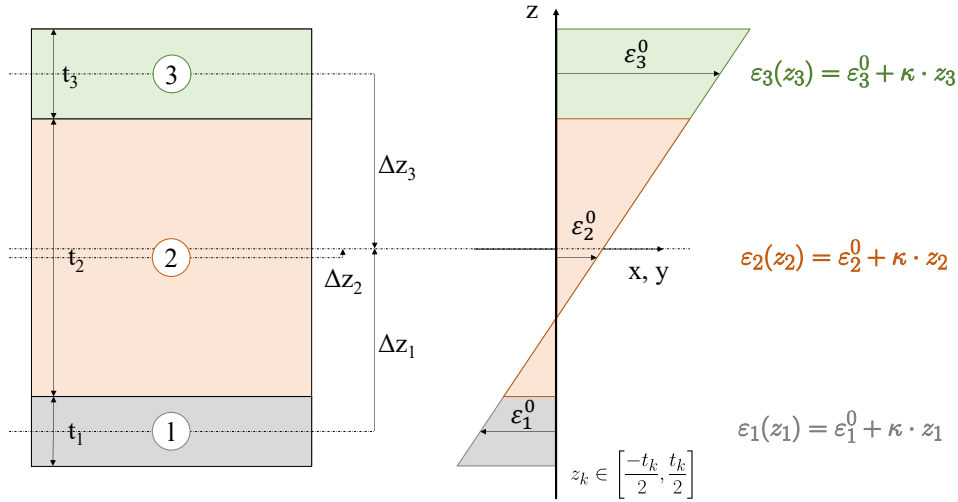
Figure 12. Strain modularization concept

4   CRC-15-240 Blade Optimization

The blade analyzed in this study is based on the structural layout of the IEA-15-240 Reference Wind Turbine. This reference
295   configuration features a blade span of approximately 117 meters and a total mass of 65 t. Structurally, the blade comprises two main spars, along with leading edge (LE) and trailing edge (TE) reinforcements, all extending from 10% to 95% of the span.

Internally, the structure combines triaxial glass fiber laminates in the outer shell with core materials that vary along span and circumference. UD Carbon laminates are used in the spar caps to provide high bending stiffness with minimal added mass, while UD Glass layers reinforce the leading and trailing edges under edgewise loading. Foam cores occupy the space between
300   spar caps and edge reinforcements beyond the root, improving buckling resistance and bending stiffness. The shear webs are also built as sandwich panels, using biaxial glass face sheets bonded to foam. Figure 13 illustrates this composition at four representative cross-sections along the blade span.

The IEA-15-240 material dataset provides a solid reference basis but contains a few undefined parameters, including Poisson's ratios for biaxial and triaxial glass laminates, as well as some missing properties for the unidirectional carbon material.
305   To enable a comprehensive structural assessment, the CRC-15-240 blade utilizes the material definitions from the IEA-22-240 Reference Wind Turbine (Zahle et al., 2024), which provides an updated dataset developed by Camarena et al. (2022). The values used in this study are summarized in Table 2.
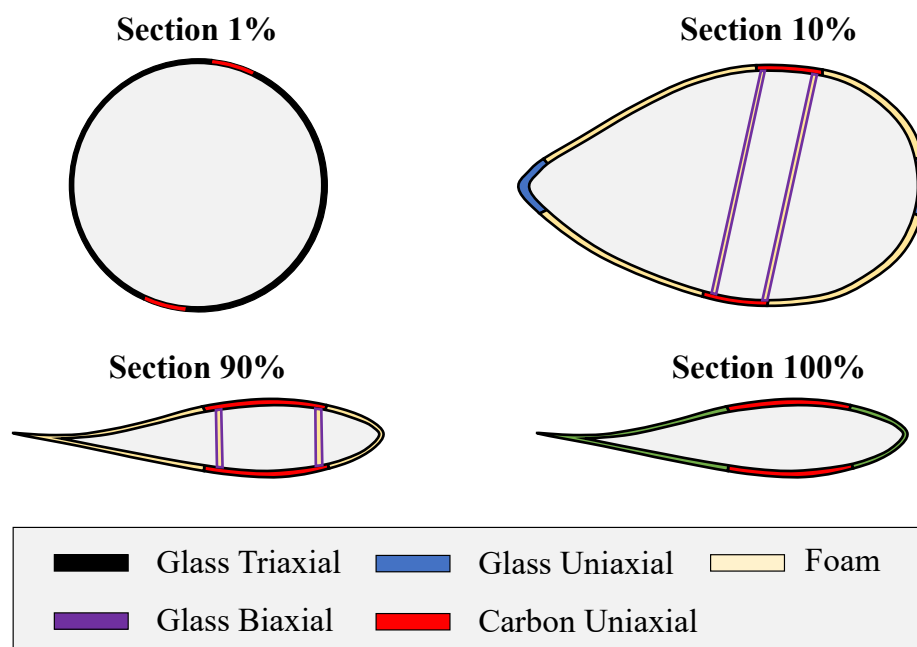
Figure 13. Cross-section schematics for different spanwise locations in the CRC-15-240 blade.

Moreover, panel-level analyses of the baseline model reveal localized instability near the blade tip, where spar caps taper and the leading and trailing edge reinforcements are discontinued, as reported by Scott et al. (2022). To mitigate this effect and
310   increase bending stiffness in these regions, the CRC-15-240 model introduces foam cores where the reinforcements are absent, thereby maintaining a continuous sandwich configuration along the blade span.

The following sections describe the complete simulation and optimization framework employed for the CRC-15-240 blade. Simulation Setup details the aeroelastic analyses, load processing procedures, and the solver–optimizer integration environment. Structural Model Initialization introduces the spanwise and circumferential discretization of the blade. Loading and
315   Boundary Conditions summarizes the design load cases and the procedure for extracting the load envelopes. Coupling and Constraints specifies the structural requirements imposed during the optimization process. Finally, Parametrization and Optimization Setup presents the parametrization strategies adopted in the analysis and provides an overview of the optimization workflow.

4.1   Simulation Setup

320   The simulation and optimization of the CRC-15-240 blade are conducted using a modular pipeline that integrates aeroelastic simulation, load processing, structural modeling, and gradient-based optimization. The overall workflow is shown in Figure 14, illustrating the data exchange between the main tools involved.

Table 2. Mechanical properties of composite and isotropic materials used in the CRC-15-240 blade. Composite values from Camarena et al. (2022).

Property	Uniaxial glass	Biaxial glass	Triaxial glass	Uniaxial carbon	Foam
E_1 [GPa]	43.70	11.02	28.21	157.6	0.1425
E_2 [GPa]	16.50	16.05	16.05	9.1	0.1425
E_3 [GPa]	15.45	16.05	15.45	9.1	0.1425
G_{12} [GPa]	3.495	3.488	3.495	4.131	–
G_{13} [GPa]	3.480	3.488	3.480	4.131	–
G_{23} [GPa]	3.480	3.488	3.480	3.488	–
ν_{12} [-]	0.35	0.345	0.345	0.30	0.3194
ν_{13} [-]	0.35	0.345	0.345	0.30	0.3194
ν_{23} [-]	0.264	0.172	0.274	0.407	0.3194
X_t [MPa]	640.23	461.24	435.65	1215.0	2.083
X_c [MPa]	–370.7	–70.69	–33.41	–878.2	1.563
Y_t [MPa]	196.10	186.4	180.0	92.1	2.083
Y_c [MPa]	–82.18	–70.69	–17.67	–38.2	1.563
S [MPa]	113.8	78.0	78.0	131.6	1.250
T [MPa]	18.97	18.97	18.97	45.4	1.250
ρ [kg/m^3]	1940	1940	1940	1600	130
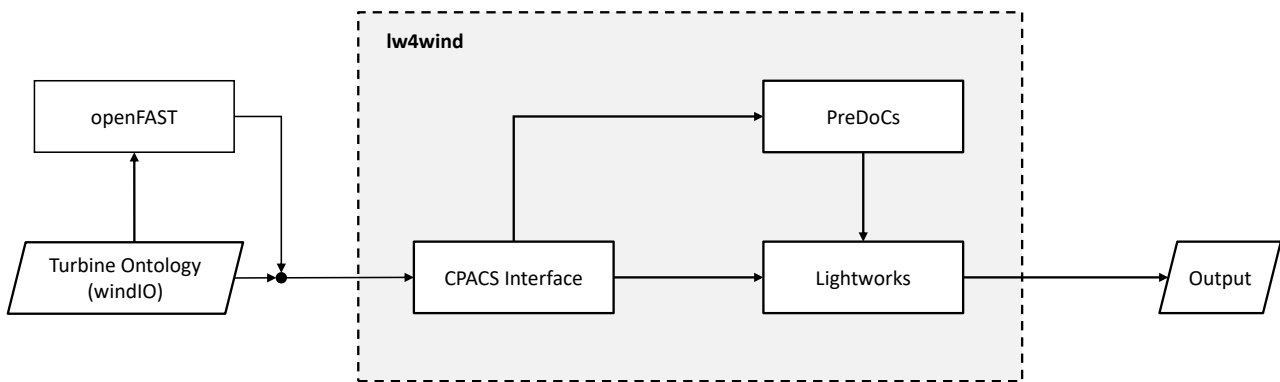
Figure 14. Simulation methodology.

At the core of this process lies the `lw4wind`[1] environment, which manages communication between all modules. The simulation begins with an aeroelastic analysis in OpenFAST, generating time series of aerodynamic and inertial loads along

---

[1] Short for "*Lightworks* for Wind"

325   the blade span. These results are then embedded into a WindIO file (Bortolotti et al. (2022)), an ontology schema that defines the storage of wind turbine engineering parameters in a hierarchical yaml structure.

      After load embedding, the pipeline proceeds to the structural modeling stage. The WindIO file is parsed through the CPACS interface, which performs the format conversion and initializes the structural solver *PreDoCS*. This stage defines the spanwise structural representation of the blade and sets up the optimization problem.

330   *PreDoCS* (Preliminary Design of Composite Structures, (Werthen et al., 2024)) performs the structural analysis of the blade as a continuous anisotropic beam governed by Timoshenko theory. During initialization, the blade span is discretized into cross-sectional stations, for which section properties and fully coupled 7×7 stiffness matrices are assembled. The solver computes the spanwise displacement field under applied external loads, from which internal loads are recovered using the cross-sectional stiffness relations described by Jung and Nagaraj (2002).

335   Once initialized, *lightworks* takes over the local structural representation, mapping each beam section to a detailed set of composite panel models. During optimization, *PreDoCS* and *lightworks* operate in parallel: *PreDoCS* provides the individual panel load states, while *lightworks* evaluates local stiffness, strength, and stability responses. Following convergence, the optimization results are post-processed.

4.2   Structural Model Initialization

340 After conversion of the blade geometry to the CPACS format, the model is segmented into structural panels. Circumferentially, each cross-section is divided into regions following WindIO conventions, which define the structural layout illustrated in Figure 13 for different span positions.

      In the spanwise direction, the blade is discretized using a two-zone uniform scheme. From the root (0–23% span), panels are spaced at 2.60 m to capture the highly loaded root region and the transition from the cylindrical base to the main blade with

345 spars. Beyond 23% span, a coarser spacing of 4.50 m is applied up to the tip, reducing computational cost while maintaining geometric continuity and manufacturability, given that taper plays in important role in composite panels design.

      In addition to spatial control, the sections are aligned with the blade's actual load axis, which follows the curved blade geometry. The resulting model is visualized in Figure 15.

4.3   Loading and Boundary Conditions

350 The loads used in this analysis represent the transient response of the nominal IEA-15-240 reference model. Aero-servo-elastic simulations are performed in OpenFAST using the ElastoDyn module, which applies an Euler–Bernoulli beam formulation with two bending modes: flapwise and edgewise deflections (Rinker et al., 2020). Building upon the structural analysis of the scaled 22 MW blade presented by Werthen et al. (2023), a reduced subset of design load cases is defined in accordance with the guidelines of DNVGL-ST-0376 (DNV GL, 2015). The selected load cases are summarized in Table 3.

355   For each load case, time series of aerodynamic and inertial loads are post-processed to extract the critical design conditions. Following the DNVGL-ST-0376 guideline (DNV GL, 2015), envelopes of all force and moment components are generated by evaluating their minimum and maximum values, including additional bending moments computed in the flap–edgewise
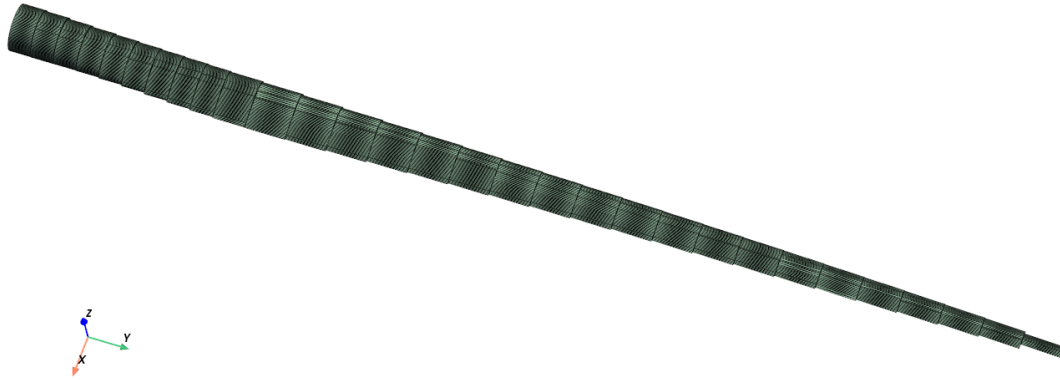
Figure 15. Structural discretization of the CRC-15-240 blade in *PreDoCS*.

Table 3. Design load cases and corresponding wind speeds used in the simulation.

DLC number	Description	Mean wind speeds (m/s)
DLC 1.5	Extreme wind shear (vertical, positive and negative horizontal wind shear)	10.6 (rated)
DLC 1.6	Power production, NTM	10, 13, 18, 21
DLC 6.1	Extreme wind, 50-year storm, yaw misalignment of $\pm 8°$	50

plane at 30° intervals from 0° to 180°. The corresponding time steps associated with the maximum flapwise and edgewise tip deflections are also included.

4.4 Coupling and Constraints

The model is subject to five categories of constraints: coupling, strength, stability, taper, and deflection. A safety factor of 1.5 is applied to all evaluated constraints, whereas coupling relations are enforced directly and therefore excluded from this factor, following the definitions adopted by Werthen et al. (2023).

Coupling relations are applied to ensure consistent material behavior across the blade. Intra-panel coupling enforces symmetry through the sandwich thickness, mirroring the outer composite about the mid-plane while maintaining the uniqueness of the core. Inter-panel coupling links corresponding composites between the upper and lower shells, ensuring material symmetry despite their geometric differences. These relations remain fixed throughout the optimization.

Strength constraints are applied at the composite level and depend on the specific class of each material. For those modeled as single-ply laminates, the Tsai-Wu criterion (Amabili, 2018) is employed. For Double-Double (DD) laminates, the Omni-

Envelope criterion is adopted, as detailed in subsection 2.3. Finally, the foam cores, due to their isotropic behavior, are evaluated using the von Mises criterion.

Stability constraints are evaluated at the panel level to account for local buckling under axial compression and in-plane shear. Assuming an orthotropic and symmetric laminate, the critical buckling load per unit width under compression is given by (Structural Analysis Working Group I, 2009, HSB-45112-02) as:

$$N_{x,\mathrm{cr}} = k_x \left(\frac{\pi}{b}\right)^2 \sqrt{\widetilde{D}_{11}\,\widetilde{D}_{22}}, \tag{23}$$

and, for shear-dominated buckling, by (Structural Analysis Working Group I, 2009, HSB-45111-08) as:

$$N_{xy,\mathrm{cr}} = k_s \left(\frac{\pi}{b}\right)^2 \sqrt[4]{D_{11}D_{22}^3}. \tag{24}$$

Here, $\widetilde{D}_{11}$ and $\widetilde{D}_{22}$ denote the laminate's effective bending stiffness terms, while k_x and k_s are the buckling coefficients for compression and shear, respectively. These coefficients are interpolated from the provided curves, assuming simply supported boundary conditions for all panel edges to yield conservative estimates.

Since both axial and shear loads act simultaneously, the overall stability assessment combines the two modes through the interaction criterion proposed by (Peters, 1954):

$$R_x + R_s^2 \leq 1, \tag{25}$$

where R denotes the ratio between the applied and critical load for each mode.

Tapering constraints prevent abrupt thickness variations between adjacent panels. All materials satisfy the DNVGL-ST-0376 requirements (DNV GL, 2015), except for the shell face sheets, which show a localized acute thickness drop near the root–mid-span transition where spars and reinforcements are introduced. Following Tsai (2021), a specific constraint is applied to the Double-Double laminates, allowing taper ratios up to $7.5\!:\!1$.

Deflection constraints are added to all use cases to limit the maximum allowable blade tip displacement under extreme load cases. These constraints ensure the tower clearance of the blades.

4.5 Parametrization and Optimization Setup

Each panel in the blade is initialized with a multi-parametric scheme that enables multi-layer sandwich configurations composed of distinct sub-components, allowing each layer to be parametrized independently. Glass unidirectional, biaxial, and unidirectional carbon laminates are modeled as transversely isotropic single plies, while the foam core is treated as isotropic. These composites are optimized solely by their thicknesses across different panels.

The main innovation is the substitution of the triaxial glass laminates with Double–Double laminates, moving from a homogenized $[0_2/\pm 45]$ stacking to a configuration composed of unidirectional glass plies, which can be tailored in thickness and stiffness through the ply angles (Φ, Ψ). To ensure consistent comparison, the baseline case also employs the DD formulation with fixed angles $[0/\pm 45]$, equivalent to the nominal triaxial stacking and part of the DD design space (Figure 2). This substitution removes inconsistencies in material properties and strength criteria, allowing all configurations to be assessed within a unified modeling approach.

Building upon this baseline, a series of simulation cases is defined with increasing levels of design freedom regarding the Double-Double skin parametrization. The different optimization scenarios are shown in Table 4.

Table 4. Comparison of Double-Double laminate configurations and variable definitions.

Config.	Description	Number of variables	Remarks
Triax	DD laminate with fixed 0°, 45° angles	1 thickness per section	Basis case, mimicking triax laminates
DD-Hard	DD laminate with fixed 0°, and Ψ variable	1 thickness per section and 1 global angle	DD with hard behavior restriction
DD	DD laminate with variable Φ and Ψ	1 thickness per section and 2 global angles	Classic DD
DD-Local	DD laminate with individualized set of angles per cross-section	1 thickness per section and 2 angles per section	Idealistic case, stiffness benchmark case

In all cases except DD-Local, the fiber angles are uniform across all panels, meaning each panel adopts the same globally optimized orientation. Only the laminate thicknesses vary along the blade span. The locally optimized case is introduced to explore the potential of angle tailoring per cross section along the blade in response to localized structural demands. While not directly manufacturable, this configuration provides insights into the maximum achievable performance through local stiffness adaptation.

An overview of the materials employed in the CRC-15-240 blade and their corresponding parametrization strategies is presented in Table 5.

Table 5. Material models and parametrization strategies in the CRC-15-240 optimization.

Material	Region	Parametrized Properties	Remarks
UD Glass	LE/TE reinf. core	Thickness	Transversely Isotropic
UD Carbon	Spar cap core	Thickness	Transversely Isotropic
Biaxial Glass	Web face sheet	Thickness	Transversely Isotropic
Foam	Web/Shell core	Thickness	Isotropic
Glass DD	Shell face sheet	Thickness, Φ, Ψ	Orthotropic

The optimization aims to minimize the total structural mass of the blade, subject to strength, stability, taper, deflection, and coupling constraints. The problem is solved using the Sparse Nonlinear OPTimizer (SNOPT), a gradient-based sequential quadratic programming algorithm that solves large-scale constrained problems through iterative quadratic approximations. Preliminary tests showed that SNOPT achieved more robust convergence than the Interior Point Optimizer (IPOPT) and the Method of Moving Asymptotes (MMA). The solver parameters follow standard definitions, except for the feasibility and optimality tolerances, which are set to 10^{-4}. For the usage of gradients, a check of the robustness of the results against varying

Table 6. Optimization formulation scheme.

	Constraint/Variable	Description	Bounds
Minimize	m	Mass of ...	
On the basis of	n_x, n_y	Panel loads (Axial forces, shear)	
With respect to	Φ in [deg]	First double double angle	$[0, 90]$
	Ψ in [deg]	Second double double angle	$[0, 90]$
Subject to	$g_{stability}$	Panel buckling	≤ 0
	$g_{strength}$	Strength Omni-FPF	≤ 0

initialization and perturbations has to be performed. Optimizations are started from different DD angle combinations like described in Zerbst et al. (2025). The mass optimum could be achieved with a reliability of over 90%. The overall optimization framework is summarized in Table 6.

420 ## 5   Results

The optimization outcomes for all design cases are summarized in Table 7. The triaxial and DD-Hard configurations yield nearly identical masses, differing by only 1.17% (839.8 kg). This indicates that the 0° plies dominate the overall stiffness, while the second angle exerts only a minor influence. In contrast, introducing full angular freedom in the DD case results in a mass reduction of 8.84% (6348.6 kg) relative to the triaxial baseline, highlighting the relevance of full directional control of the

425 fiber orientations. The DD-Local case, which permits section-wise variation of Φ and Ψ, achieves only a marginal additional improvement of 1.38% (901.5 kg) compared to the DD case, demonstrating that the globally optimized configuration already captures most of the achievable gains.

Table 7. Comparison of mass and optimized angles for each design case.

Parameter	Triax	DD-Hard	DD	DD-Local
Mass [t]	71.834	70.995	65.486	64.585
Φ [deg]	0	0	48	–
Ψ [deg]	45	49.2	48	–

Regarding the optimized fiber orientations, the results indicate a general shift toward laminates favoring buckling and shear resistance, typically characterized by plies around 45°. This trend is illustrated in Figure 16, which shows the stiffness of each

430 configuration in the lamination parameter design space.
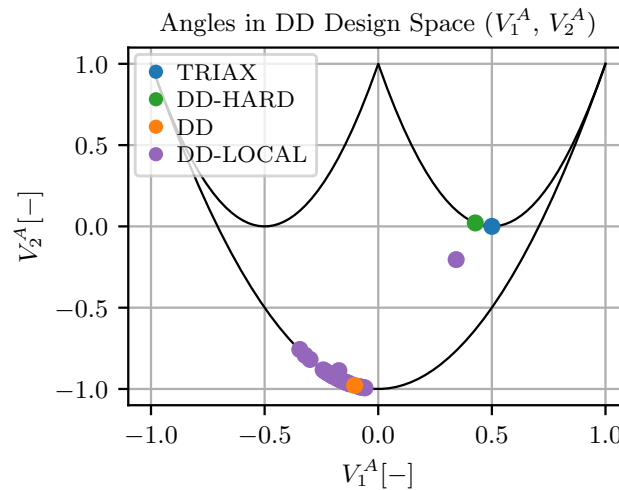
Figure 16. Case-related stiffness in LP design space

The Triax configuration remains fixed, while the DD-Hard model slightly increases the second angle to reduce axial stiffness along the span. Despite this adjustment, both configurations exhibit similar stiffness behavior, positioned within the "hard" region identified by Tsai (2021). This explains the marginal difference in their optimized masses, as the limited variation of approximately $4.2°$ in the second angle produces minimal stiffness changes.

435   In contrast, the DD case, where both angles are freely optimized, is driven toward the softest region of the lamination parameter space, centered around $\pm45°$ and near the lower boundary of the feasible domain. This outcome reflects a clear preference for shear- and buckling-dominated behavior, with Φ and Ψ converging to approximately $48°$. A comparable pattern appears in the DD-Local case, where the section-wise optimized angles cluster within the same soft region, confirming the consistency of the global DD solution.

440   The spanwise mass distribution for all configurations is presented in Figure 17. The influence of laminate stiffness tailoring is evident: shell stiffness directly governs the structural mass profile. The Triax and DD-Hard cases exhibit nearly identical distributions near the root, with a slight divergence emerging beyond mid-span due to the enhanced shear and buckling resistance of the DD-Hard laminates.

Nevertheless, the total mass difference between the Triax and DD cases amounts to 6348.6 kg. The root region, marked by a

445   significant mass drop, accounts for approximately 64% of the total reduction (4066.6 kg), while the remaining 36% (2282 kg) is distributed along the mid-span and tip. This concentration of mass reduction near the root highlights its dominant role in the optimization, driven by the region's structural simplicity and exposure to high loads. It consists solely of two spar-cap cores and two face-sheet layers, making it highly sensitive to stiffness adjustments.

Between the DD and DD-Local models, a distinct trend emerges: the DD configuration achieves lower mass near the root,

450   while the DD-Local model performs slightly better toward the mid-span. This behavior reflects the additional flexibility of the
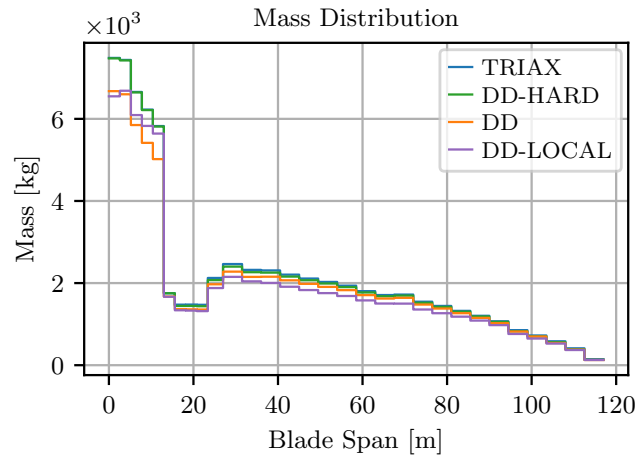
Figure 17. Spanwise distribution of mass.

DD-Local setup, which allows localized stiffness adaptation but yields only marginal overall improvement. Similarly, the DD-Hard configuration shows limited gains relative to the triaxial baseline. As both variants primarily serve as boundary references for the Double-Double formulation, the following analysis focuses on comparing the Triax and DD cases.

5.1 Comparative Analysis of Triaxial and Double-Double Configurations

455 To better interpret the influence of laminate architecture on the mass distribution, the thickness profiles provide a clear physical indication. Figure 18 compares the spar-cap core and shell-skin thicknesses for the Triax and DD configurations. Near the root, within the cylindrical section, the $[0_2, \pm45]$ layup exhibits consistently thicker components than the $[\pm48, \pm48]$ configuration: about 36.4% greater CFRP-core thickness and 9% greater GFRP-skin thickness in the first section. This highlights how the laminate orientation affects not only its own stiffness but also the material demand in adjacent layers.

460 After the cylindrical sections, the shell skin thickness shows a progressive loss of structural relevance, as spars and edge reinforcements assume the primary load-bearing function. A marked reduction occurs at the 6th section, limited by the tapering ratio 7.5. For the triaxial skin, the thickness decreases from 37.2 mm to 5.0 mm over the local span; for the DD configuration, it decreases from 31.7 mm to 4.2 mm, both matching the allowable slope. By the 7th section, both skins attain their minimum allowable thicknesses: 2.0 mm for the Triax and 1.5 mm for the DD configuration, corresponding to four and three plies,

465 respectively. The larger minimum thickness of the Triax skin results in locally higher bending stiffness, which slightly reduces the spar-cap demand but does not improve the overall mass efficiency of the section, as inferred from Figure 17.

Given the relevance of the root section in terms of mass contribution and the strong influence of DD angles, this region is analyzed in more detail. The stiffer the laminate is in the direction of load application, the greater the expected concentration
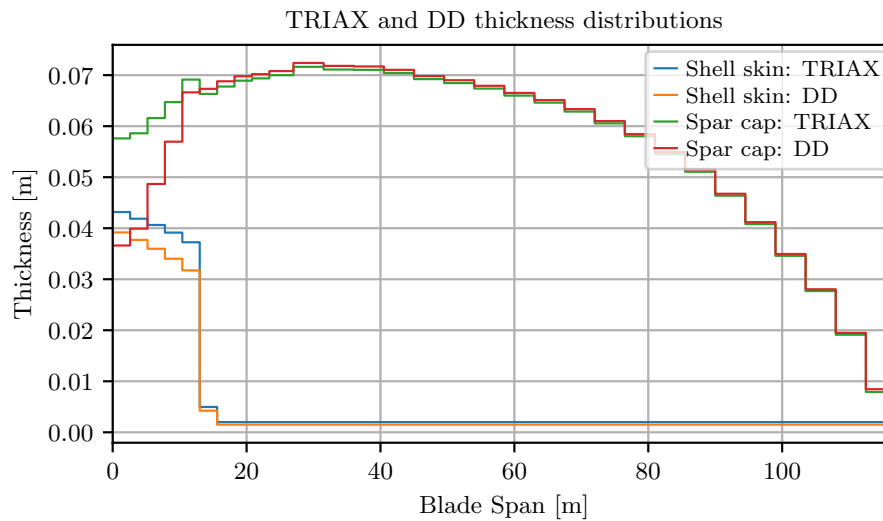
Figure 18. Thickness distribution of spar cap core and shell skin

of membrane forces. This effect is evident in Figure 19, where axial loads N_x concentrate within the spar-cap region due to the

470   thick unidirectional CFRP layers.
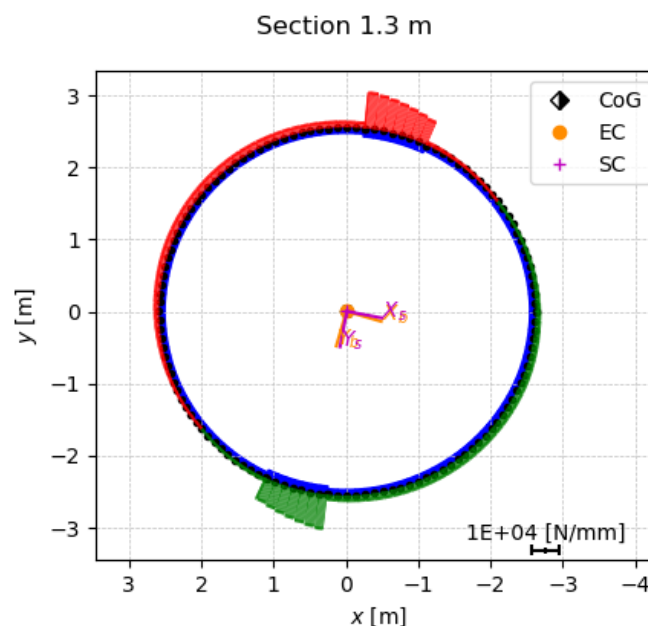
Figure 19. Axial force distribution (N_x) for the critical minimum edgewise moment case (Triax and DD).

However, the triaxial laminates contain a larger portion of $0°$ plies, which concentrate excessive axial stiffness in the face sheets. Considering the superior strength-to-weight ratio of CFRP and the structural role of the spar cap, this behavior contradicts the most efficient stiffness distribution. As shown in Figure 20, the spar cap remains far from the constraint threshold of 0, while the shell operates at its limits under buckling criteria. Consequently, the optimizer first increases the spar-cap thickness

475 to relieve part of the load carried by the shell, which acts as a sinking component. In addition, the $0°$-dominated layup provides poor buckling resistance, further requiring local thickening of both the spar-cap core and shell face sheets. Conversely, the $[\pm48, \pm48]$ configuration, with its lower axial stiffness and improved buckling compliance, reduces the spar-cap demand for load redistribution and is inherently thinner.
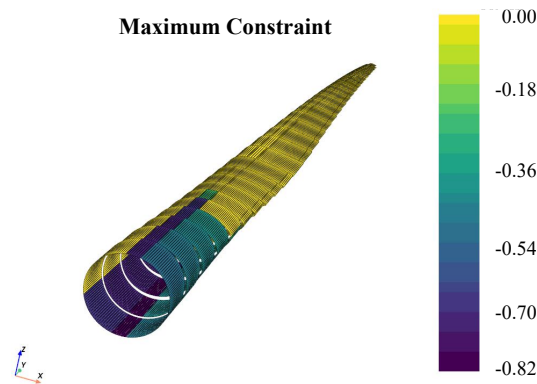
Figure 20. Constraint contour distribution for the Triax case.

Figure 21 summarizes the interaction between shell skins and spar-cap core, illustrating the feedback process responsible

480 for the inferior structural response of the triaxial laminate in the root region.
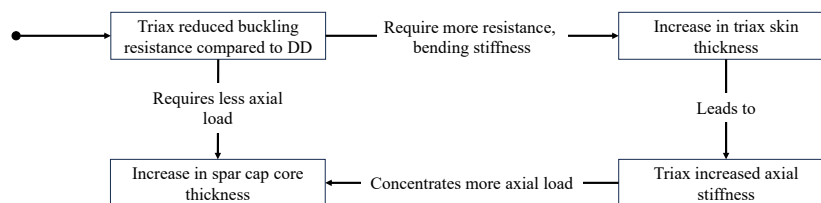
Figure 21. Interaction between Triax skin and spar cap core response.

In terms of trailing and leading edge reinforcements, as shown in Figure 22, they follow a similar overall trend for both the Triax and DD configurations. Reinforcements are generally thinner in the Triax case, primarily due to the additional axial stiffness provided by the 0-degree plies in the skin. In contrast, the DD configuration lacks this axial reinforcement from the skin, and the UD core must compensate for this, resulting in thicker reinforcements.
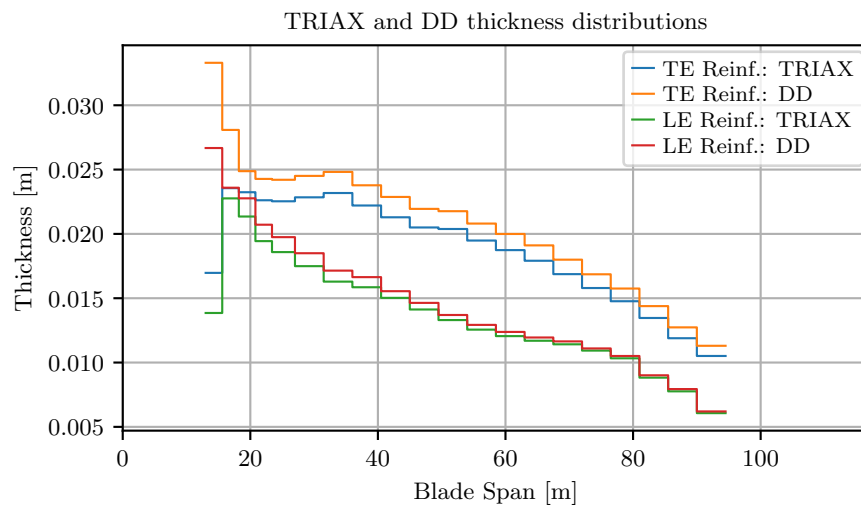
Figure 22. Thickness distribution of TE and LE reinforcements
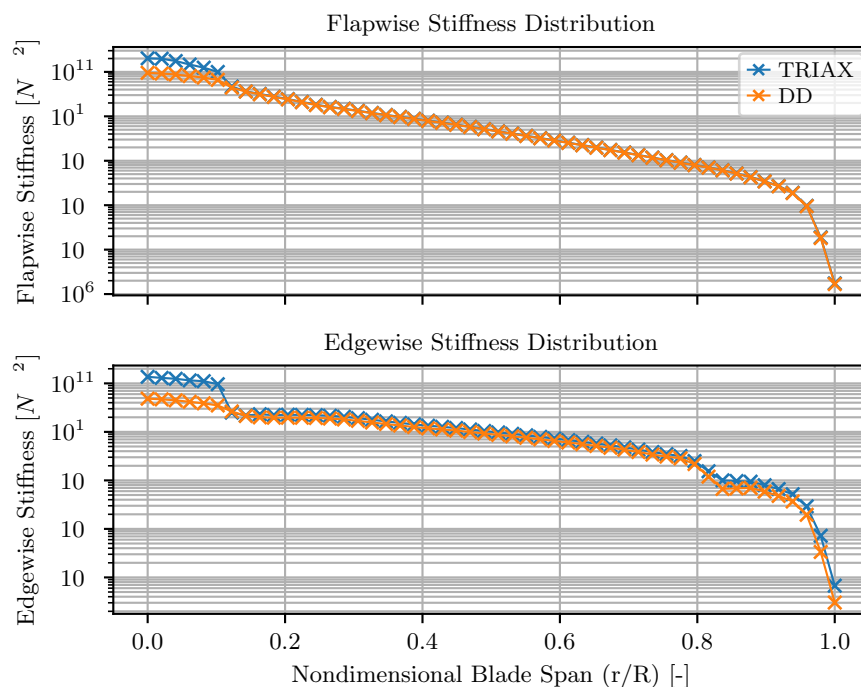
Figure 23. Flapwise (upper) and edgewise (lower) stiffness distributions for both configurations.

485   The most pronounced differences occur at the beginning of the reinforcement regions, around the 6th section, where the Triax reinforcements start from lower thicknesses. This behavior results from the combination of tapering constraints and strength-driven sizing: the stiffer Triax skin, dominated by 0° plies, carries part of the axial load that would otherwise be absorbed by the reinforcements. Conversely, the softer DD skin ($\pm48°$) transfers greater axial demand to the cores, requiring locally thicker reinforcements. Beyond this zone, buckling becomes dominant, leading to a less pronounced thickness offset between

490 configurations, as the triax contribution of 0-degree layers is less efficient.

    Given the redistribution of loads between shell skins, spar-cap cores, and LE/TE reinforcements, spanwise variations in blade stiffness are expected. As shown in Figure 23, the largest difference in flapwise stiffness occurs near the root, where the DD is softer due to its reduced spar-cap thickness. Beyond this region, the spar-cap thicknesses in both configurations converge, leading to similar stiffness trends along the remaining span. In contrast, the edgewise stiffness distribution exhibits a larger

495 root-region offset, even though both configurations converge along the span. In edgewise bending, the spar cap contributes less to stiffness, shifting the dominant role to the reinforcements and shell skins. The Triax skin, with its higher axial stiffness, therefore provides greater support, particularly at the root and near the tip where LE and TE reinforcements terminate. In these regions, the skin dominates the edgewise response.

5.2   In-Depth Analysis of the Optimized Double-Double Blade

500 Near the root (Figure 24), the configuration reveals a structurally simple yet heavily reinforced section. The high material density in this region reflects its critical role in load transfer, particularly through the spar cap and shell skin. The skin plays a dominant role in this area and benefits the most from optimization, as previously discussed.

    Progressing outward, Figure 25 illustrates the transition in structural composition with the introduction of foam cores, UD Glass reinforcements, and the shear webs. Among the layups originating from the root, only the spar cap core maintains the

505 same thickness distribution trend. In contrast, the shell skin rapidly decreases in thickness and structural relevance, in line with the shift toward spar- and reinforcement-dominated load paths.

    The section at 83 % span, shown in Figure 26 illustrate the increasingly simplified structural layout of the blade as it approaches the tip. The introduction of foam at the leading and trailing edges reflects a modification incorporated into the CRC-15 blade to enhance local bending stiffness in a region where the UD glass is already tapered out. Notably, the foam

510 cores are not reduced to their minimum allowable thickness, indicating their structural relevance in mass saving.

    A key characteristic of the IEA-15-240 design is its material symmetry between the pressure and suction sides. Although the outer geometry is aerodynamically asymmetric, each structural panel on the upper surface has a mirrored counterpart on the lower side. Under asymmetric operational loading, particularly flapwise bending, the suction side experiences higher compressive stresses and therefore becomes a critical factor in design. As widely reported in the literature (Ullah et al., 2020),

515 this region is more susceptible to buckling, which typically governs the sizing of large wind turbine blades.

    In the CRC simulations, the suction-side panels govern the structural sizing along the span due to the dominant compressive demand imposed by bending. The spar caps are constrained by the peak flapwise moment, while the leading and trailing edges are governed by combined flapwise–edgewise load cases. The leading edge is placed in compression under the 150-
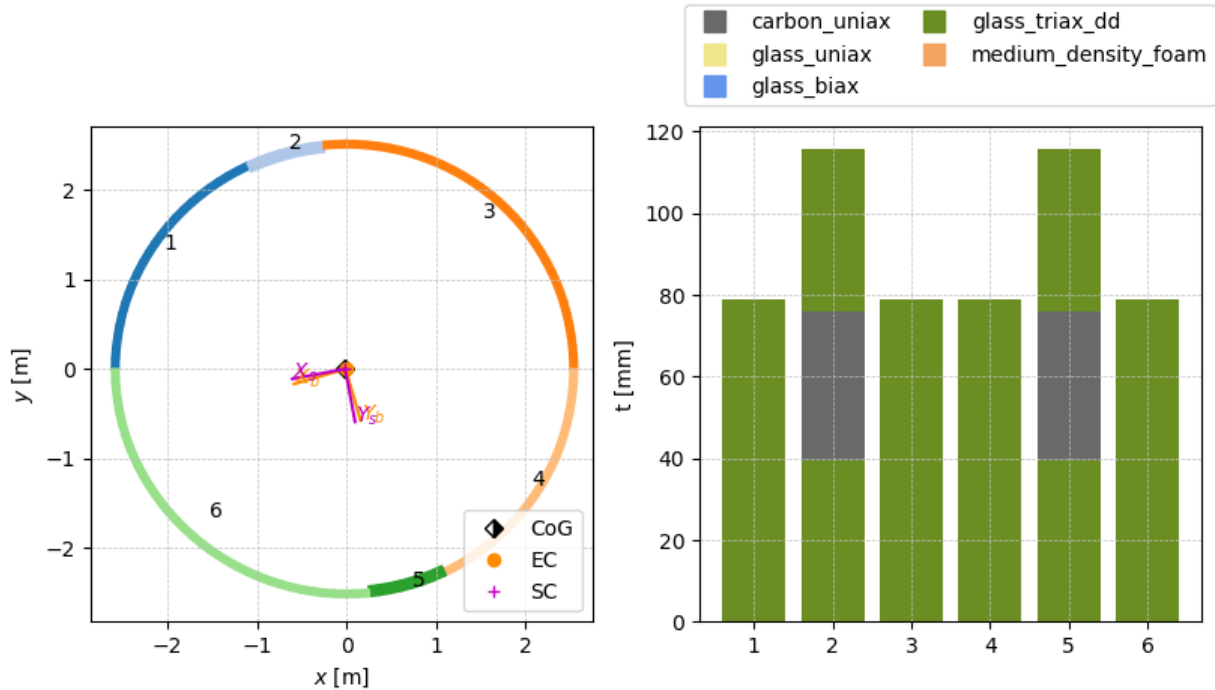
Figure 24. Section at 1% span.

degree moment orientation, whereas the trailing edge is compressed under the 30-degree orientation, which reverses the ten-
sion–compression distribution between the two regions. This loading pattern establishes compression-induced buckling as the
primary sizing mechanism across the suction-side panels, confirming that the DD configuration operates in the same regime.
The tailored $\pm48°$ laminate angles align more effectively with the principal load paths than the triaxial layup, whose higher
axial stiffness interacts less efficiently with the spar caps and edge reinforcements.

6 Conclusions

This work introduced a multi-parametric panel approach and incorporated it into the blade-optimization workflow, enabling
sandwich panels to be represented as modular assemblies with independently parameterized materials. The formulation was
verified through stiffness, load-path, and tapering consistency tests, establishing its suitability for applying continuous compos-
ite descriptions. This capability enabled the examination of Double-Double laminates as viable replacements for conventional
triaxial skins in a large-scale optimization setting.

With this, the optimization of the CRC-15-240 blade using Double-Double laminates resulted in a mass reduction of 8.84%,
equivalent to 6,348.6 kg, compared to the baseline triaxial configuration. This improvement was achieved by replacing the
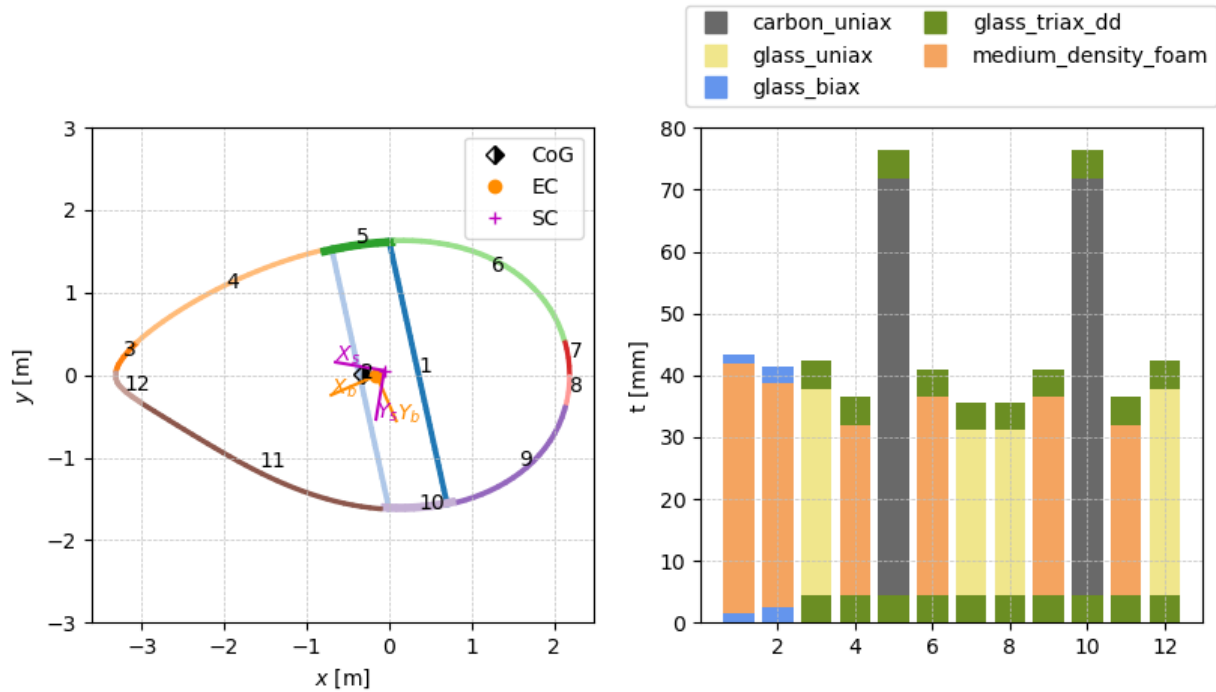
Figure 25. Section at 12% span.
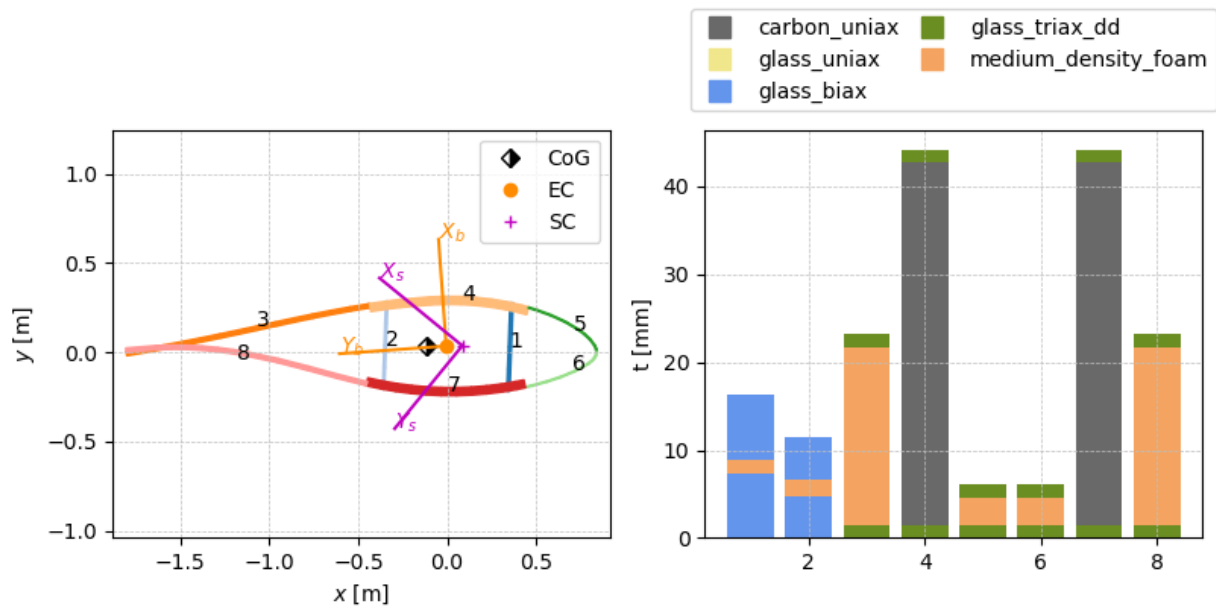
Figure 26. Section at 83% span.

original triaxial skins with laminates based on a $[\pm 48°/\pm 48°]$ building block. The resulting configuration shifted the skin response from an axially stiff regime to a softer one, better suited to resisting shear and buckling.

Although $45°$ layers are generally optimal for such loading conditions, the optimized configuration converged toward slightly higher off-axis angles. Two main factors explain this tendency. First, the interaction between shear and compression loads benefits from stress redistribution within the layer matrix. Second, the solver implicitly sought to reduce flapwise bending stiffness, favoring higher off-axis orientations and maximizing the use of unidirectional carbon fiber, which offers superior strength-to-weight performance.

Beyond the spar caps, the upper skin emerged as the dominant sizing region. This area experienced the highest stresses, particularly in compression, which were identified as the primary failure mode. These trends align with the findings of Zerbst et al. (2025), who observed similar angle convergence in the upper panels of an aircraft wing optimized with Double-Double laminates. In both cases, the upper skins developed greater thicknesses and converged toward comparable orientations, reinforcing the physical plausibility of the simulated results.

From a stiffness perspective, the aeroelastic response was only moderately affected. The most significant variations occurred near the blade root, where local mass reductions reached approximately 64%. Despite these changes, all flapwise and edgewise displacements remained within the operational limits defined in Gaertner et al. (2020), confirming the structural viability of the optimized design.

From a manufacturing standpoint, the optimized Double-Double skins integrate seamlessly into existing blade production practices. In a manner consistent with triaxial laminates, they can be assembled as repeating blocks, but with two selected fiber angles arranged according to the Double-Double stacking pattern. This configuration remains fully compatible with current fabrics and vacuum-infusion processes and does not introduce any additional layup complexity. Consequently, the Double-Double concept offers a practical approach to achieving weight savings while maintaining the established workflow used for conventional triaxial skins.

6.1 Future Work

Several research directions naturally extend from this work. First, integrating a fully coupled aeroelastic analysis into the optimization pipeline would enable more accurate prediction of stiffness-induced load redistribution. The current formulation assumes fixed aerodynamic loading and therefore does not capture secondary effects arising from skin softening or stiffness variation.

Second, fatigue modeling is a key area for further work. Double-Double laminates are relatively new and lack extensive experimental data, so their long-term cyclic performance remains uncertain. Future research should integrate simplified fatigue degradation models into the optimization process and support experiments to characterize endurance. These data would allow direct fatigue constraints in the design space and, when needed, guide limits on allowable configurations. Nevertheless, preliminary tension–compression fatigue tests, such as those in Vasconcelos et al. (2025), indicate that Double-Double laminates retain structural integrity under cyclic loading, supporting their long-term use.

Appendix A: Derivation of Plane-Shifted Stiffness Matrices

565

Extension Stiffness:

$$[\mathbf{A}^{\text{new}}] = \sum_k [\bar{\mathbf{Q}}_k] \left[z_{k-1}^{\text{new}} - z_k^{\text{new}} \right]$$

$$= \sum_k [\bar{\mathbf{Q}}_k] \left[(z_{k-1}^0 - \Delta z) - (z_k^0 - \Delta z) \right]$$

$$= \underbrace{\sum_k [\bar{\mathbf{Q}}_k] \left[z_{k-1}^0 - z_k^0 \right]}_{\mathbf{A}^0}$$

$$= [\mathbf{A}^0]$$

Bending–Extension Stiffness:

$$[\mathbf{B}^{\text{new}}] = -\frac{1}{2} \sum_k [\bar{\mathbf{Q}}_k] \left[(z_{k-1}^{\text{new}})^2 - (z_k^{\text{new}})^2 \right]$$

$$= -\frac{1}{2} \sum_k [\bar{\mathbf{Q}}_k] \left[(z_{k-1}^0 - \Delta z)^2 - (z_k^0 - \Delta z)^2 \right]$$

$$= -\frac{1}{2} \sum_k [\bar{\mathbf{Q}}_k] \left[(z_{k-1}^0)^2 - 2z_{k-1}^0 \Delta z + \Delta z^2 \right]$$

$$+ \frac{1}{2} \sum_k [\bar{\mathbf{Q}}_k] \left[(z_k^0)^2 - 2z_k^0 \Delta z + \Delta z^2 \right]$$

$$= \underbrace{-\frac{1}{2} \sum_k [\bar{\mathbf{Q}}_k] \left[(z_{k-1}^0)^2 - (z_k^0)^2 \right]}_{\mathbf{B}^0}$$

$$+ \Delta z \underbrace{\sum_k [\bar{\mathbf{Q}}_k] \left[z_{k-1}^0 - z_k^0 \right]}_{\mathbf{A}^0}$$

$$= [\mathbf{B}^0] + \Delta z [\mathbf{A}^0].$$

570 Bending Stiffness:

$$[\mathbf{D}^{\text{new}}] = \frac{1}{3}\sum_k [\bar{\mathbf{Q}}_k]\left[(z_{k-1}^{\text{new}})^3 - (z_k^{\text{new}})^3\right]$$

$$= \frac{1}{3}\sum_k [\bar{\mathbf{Q}}_k]\left[(z_{k-1}^0 - \Delta z)^3 - (z_k^0 - \Delta z)^3\right]$$

$$= \frac{1}{3}\sum_k [\bar{\mathbf{Q}}_k]\Big\{(z_{k-1}^0)^3 - 3\Delta z(z_{k-1}^0)^2 + 3\Delta z^2 z_{k-1}^0$$

$$\quad - \Delta z^3 - \left[(z_k^0)^3 - 3\Delta z(z_k^0)^2 + 3\Delta z^2 z_k^0 - \Delta z^3\right]\Big\}$$

$$= \underbrace{\frac{1}{3}\sum_k [\bar{\mathbf{Q}}_k]\left[(z_{k-1}^0)^3 - (z_k^0)^3\right]}_{\mathbf{D}^0}$$

$$+ 2\Delta z\underbrace{\left(-\frac{1}{2}\sum_k [\bar{\mathbf{Q}}_k]\left[(z_{k-1}^0)^2 - (z_k^0)^2\right]\right)}_{\mathbf{B}^0}$$

$$+ \Delta z^2\underbrace{\sum_k [\bar{\mathbf{Q}}_k]\left[z_{k-1}^0 - z_k^0\right]}_{\mathbf{A}^0}$$

$$= [\mathbf{D}^0] + 2\Delta z\,[\mathbf{B}^0] + \Delta z^2\,[\mathbf{A}^0].$$

Data availability. The raw data required to reproduce these findings are available under the following repository: https://doi.org/10.5281/zenodo.17965770 (Werthen, 2025).

Author contributions. EW and GNR developed the methodology and software code, did the analyses and wrote the manuscript. SD and LT
575 supported the implementation of the approach into the *lightworks* framework. DZ and CH revised the manuscript and provided scientific supervision.

Competing interests. The authors declare that they have no known competing financial interests or personal relationships that could have appeared to influence the work reported in this paper.

Acknowledgements. We would like to acknowledge the funding by the Deutsche Forschungsgemeinschaft (DFG, German Research Foun-
580 dation) under Germany´s Collaborative Research Center – CRC 1463/2 - Integrated design and operation methodology for offshore megas-tructures – Project-ID 434502799.

References

Almeida, J. H. S., Balonek, E., and Castro, S. G.: Beyond Double-Double theory: n-Directional stacking sequence optimisation in composite laminates, Composite Structures, 373, 119 586, https://doi.org/https://doi.org/10.1016/j.compstruct.2025.119586, 2025.

585 Amabili, M.: Composite, Sandwich and Functionally Graded Materials: Advanced Nonlinear Shell Theories, p. 90–123, Cambridge University Press, 2018.

Bak, C., Zahle, F., Bitsche, R., Kim, T., Yde, A., Henriksen, L., Hansen, M., Blasques, J., Gaunaa, M., and Natarajan, A.: The DTU 10-MW Reference Wind Turbine, danish Wind Power Research 2013 ; Conference date: 27-05-2013 Through 28-05-2013, 2013.

Bortolotti, P., Tarrés, H., Dykes, K., Merz, K., Sethuraman, L., Verelst, D., and Zahle, F.: IEA Wind TCP Task 37: Systems Engineering in
590 Wind Energy-WP2.1 Reference Wind Turbines, National Renewable Energy Laboratory (NREL), https://doi.org/10.2172/1529216, 2019.

Bortolotti, P., Bay, C., Barter, G., Gaertner, E., Dykes, K., McWilliam, M., Friis-Moller, M., Pedersen, M. M., and Zahle, F.: *System Modeling Frameworks for Wind Turbines and Plants: Review and Requirements Specifications*, Tech. rep., https://doi.org/10.2172/1868328, 2022.

Camarena, E., Anderson, E., Paquette, J., Bortolotti, P., Feil, R., and Johnson, N.: Land-based wind turbines with flexible rail-transportable blades – Part 2: 3D finite element design optimization of the rotor blades, Wind Energy Science, 7, 19–35, https://doi.org/10.5194/wes-7-
595 19-2022, 2022.

Castro, O.: Fatigue strength of composite wind turbine blade structures, Ph.D. thesis, Denmark, https://doi.org/10.11581/00000037, 2018.

Couto, L. d. L., Moreira, N. E., Saito, J. Y. d. O., Hallak, P. H., and Lemonge, A. C. d. C.: Multi-Objective Structural Optimization of a Composite Wind Turbine Blade Considering Natural Frequencies of Vibration and Global Stability, Energies, 16, https://doi.org/10.3390/en16083363, 2023.

600 Dähne, S., Werthen, E., Zerbst, D., Tönjes, L., Traub, H., and Hühne, C.: Lightworks, a scientific research framework for the design of stiffened composite-panel structures using gradient-based optimization, Structural and Multidisciplinary Optimization, 67, 70, https://doi.org/10.1007/s00158-024-03783-1, 2024.

Daniel, I., Werner, B., and Fenner, J.: Strain-rate-dependent failure criteria for composites, Composites Science and Technology, 71, 357–364, https://doi.org/https://doi.org/10.1016/j.compscitech.2010.11.028, 2011.

605 DNV GL: DNVGL-ST-0376: Rotor Blades for Wind Turbines, Standard, Proposal No. 2015-218, Final Draft for Hearing, published by DNV GL Renewables Certification, 2015.

Gaertner, E., Rinker, J., Sethuraman, L., Zahle, F., Anderson, B., Barter, G., Abbas, N., Meng, F., Bortolotti, P., Skrzypinski, W., Scott, G., Feil, R., Bredmose, H., Dykes, K., Sheilds, M., Allen, C., and Viselli, A.: Definition of the IEA 15-Megawatt Offshore Reference Wind Turbine, Tech. rep., International Energy Agency, https://www.nrel.gov/docs/fy20osti/75698.pdf, 2020.

610 Garofano, A., Sellitto, A., Acanfora, V., Di Caprio, F., and Riccio, A.: On the effectiveness of double-double design on crashworthiness of fuselage barrel, Aerospace Science and Technology, 140, 108 479, https://doi.org/https://doi.org/10.1016/j.ast.2023.108479, 2023.

Gasch, R. and Twele, J.: Wind Power Plants: Fundamentals, Design, Construction and Operation, Springer Berlin Heidelberg, Berlin, Heidelberg, 2nd ed. 2012 edn., ISBN 978-3-642-22937-4, 2012.

Hayat, K., Siddique, S., Sultan, T., Ali, H. T., Aloufi, F. A., and Halawani, R. F.: Effect of Spar Design Optimization on the Mass and Cost
615 of a Large-Scale Composite Wind Turbine Blade, Energies, 15, https://doi.org/10.3390/en15155612, 2022.

Jung, S. and Nagaraj, V. T.: Structural Behavior of Thin- and Thick-Walled Composite Blades with Multi-Cell Sections, in: 43rd AIAA/ASME/ASCE/AHS/ASC Structures, Structural Dynamics, and Materials Conference, American Institute of Aeronautics and Astronautics, https://doi.org/10.2514/6.2002-1432, structures, Structural Dynamics, and Materials and Co-located Conferences, 2002.

Kappel, E.: Double–Double laminates for aerospace applications — Finding best laminates for given load sets, Composites Part C: Open
  Access, 8, 100 244, https://doi.org/https://doi.org/10.1016/j.jcomc.2022.100244, 2022.

Kappel, E.: On invariant combinations of Qij coefficients and a novel invariant IQ, Composites Part C: Open Access, 10, 100 335,
  https://doi.org/https://doi.org/10.1016/j.jcomc.2022.100335, 2023.

Kappel, E. and Tsai, S. W.: Double-Double Laminates - A Review on the Status Quo in Spring 2024, Tech. rep., DLR (German Aerospace
  Center), https://elib.dlr.de/204753/, published under Clean Aviation, UpWing, 2024.

Kappel, E., Boose, Y., and Mißbach, M.: A CAI study on transition zones of conventional and Double-Double laminates, Composites Part
  C: Open Access, 14, 100 450, https://doi.org/https://doi.org/10.1016/j.jcomc.2024.100450, 2024.

Liu, P. and Barlow, C. Y.: Wind turbine blade waste in 2050, Waste Management, 62, 229–240,
  https://doi.org/https://doi.org/10.1016/j.wasman.2017.02.007, 2017.

Mishnaevsky, L., Branner, K., Petersen, H. N., Beauson, J., McGugan, M., and Sørensen, B. F.: Materials for Wind Turbine Blades: An
  Overview, Materials, 10, https://doi.org/10.3390/ma10111285, 2017.

Nettles, A. T.: Basic mechanics of laminated composite plates, Tech. rep., National Aeronautics and Space Administration, Huntsville, AL
  (United States). George C. Marshall Space Flight Center, https://www.osti.gov/biblio/6880327, 1994.

Peters, R. W.: Buckling of Long Square Tubes in Combined Compression and Torsion and Comparison with Flat-plate Buckling Theories,
  Technical Note NACA-TN-3184, National Advisory Committee for Aeronautics (NACA), https://ntrs.nasa.gov/citations/19930083964,
  public domain. Work of the U.S. Government. Public use permitted, 1954.

Rinker, J. and Dykes, K. L.: WindPACT Reference Wind Turbines, Tech. rep., National Renewable Energy Laboratory (NREL), Golden, CO
  (United States), https://doi.org/10.2172/1432194, 2018.

Rinker, J., Gaertner, E., Zahle, F., Skrzypiński, W., Abbas, N., Bredmose, H., Barter, G., and Dykes, K.: Comparison of loads from
  HAWC2 and OpenFAST for the IEA Wind 15 MW Reference Wind Turbine, Journal of Physics: Conference Series, 1618, 052 052,
  https://doi.org/10.1088/1742-6596/1618/5/052052, 2020.

Rosemeier, M. and Krimmer, A.: Rotorblattstruktur, in: Einführung in die Windenergietechnik, edited by Schaffarczyk, A. P., chap. 5, pp.
  169–220, Carl Hanser Verlag GmbH & Co. KG, 3 edn., ISBN 9783446473225, https://doi.org/10.1007/978-3-446-47322-5, 2022.

Samborsky, D. D. and Mandell, J. F.: Fatigue resistant fiberglass laminates for wind turbine blades, American Society of Mechanical Engi-
  neers, New York, NY (United States), https://www.osti.gov/biblio/372115, 1996.

Scott, S., Greaves, P., Macquart, T., and Pirrera, A.: Comparison of blade optimisation strategies for the IEA 15MW reference turbine, Journal
  of Physics: Conference Series, 2265, 032 029, https://doi.org/10.1088/1742-6596/2265/3/032029, 2022.

Serafeim, G. P., Manolas, D. I., Riziotis, V. A., Chaviaropoulos, P. K., and Saravanos, D. A.: Optimized blade mass reduction of a 10MW-
  scale wind turbine via combined application of passive control techniques based on flap-edge and bend-twist coupling effects, Journal of
  Wind Engineering and Industrial Aerodynamics, 225, 105 002, https://doi.org/https://doi.org/10.1016/j.jweia.2022.105002, 2022.

Sjølund, J. H. and Lund, E.: Structural Gradient-Based Sizing Optimization of Wind Turbine Blades with Fixed Outer Geometry, Composite
  Structures, 203, 725–739, https://doi.org/10.1016/j.compstruct.2018.07.031, 2018.

Structural Analysis Working Group I: Luftfahrttechnisches Handbuch für Strukturberechnung (HSB), IASB (Industrie Ausschuss Struktur
  Berechnungsunterlagen), DASA-Airbus, Bremen, available in German and English at the Technical Information Library (TIB), Hannover,
  2009.

Tsai, S. and Melo, J.: Composite Materials Design and Testing: Unlocking Mystery with Invariants, Stanford Aeronautics & Astronautics,
  ISBN 9780986084515, https://books.google.de/books?id=pLxsrgEACAAJ, 2015a.

Tsai, S. and Melo, J.: Composite Materials Design and Testing: Unlocking Mystery with Invariants, Stanford Aeronautics & Astronautics, ISBN 9780986084508, https://books.google.com.br/books?id=ykBrrgEACAAJ, 2015b.

Tsai, S. W.: Double–Double: New Family of Composite Laminates, AIAA Journal, 59, 4293–4305, https://doi.org/10.2514/1.J060659, 2021.

660 Ullah, H., Ullah, B., and Silberschmidt, V. V.: Structural integrity analysis and damage assessment of a long composite wind turbine blade under extreme loading, Composite Structures, 246, 112 426, https://doi.org/https://doi.org/10.1016/j.compstruct.2020.112426, 2020.

Vasconcelos, T. B., Alves, J. L. C., da Costa Ferreira, E. P., Júnior, R. C. S. F., and Melo, J. D. D.: Static and fatigue behavior of double-double glass/epoxy laminates, Journal of Composite Materials, 59, 119–133, https://doi.org/10.1177/00219983241261065, 2025.

Werthen, E.: CRC1463 Blade designs with double-double laminates for the CRC15-240 turbine, https://doi.org/10.5281/zenodo.17965770,
665 2025.

Werthen, E., Ribnitzky, D., Zerbst, D., Kühn, M., and Hühne, C.: Aero-structural coupled optimization of a rotor blade for an upscaled 25 MW reference wind turbine, Journal of Physics: Conference Series, 2626, 012 012, https://doi.org/10.1088/1742-6596/2626/1/012012, 2023.

Werthen, E., Hardt, D., Balzani, C., and Hühne, C.: Comparison of different cross-sectional approaches for the structural design and opti-
670 mization of composite wind turbine blades based on beam models, Wind Energy Science, 9, 1465–1481, https://doi.org/10.5194/wes-9-1465-2024, 2024.

Zahle, F., Barlas, A., Lønbæk, K., Bortolotti, P., Zalkind, D., Wang, L., Labuschagne, C., Sethuraman, L., and Barter, G.: Definition of the IEA Wind 22-Megawatt Offshore Reference Wind Turbine, Tech. Rep. DTU Wind Report E-0243, https://doi.org/10.11581/DTU.00000317, Technical University of Denmark, International Energy Agency, ISBN 978-87-87335-71-3, 2024.

675 Zerbst, D., Tönjes, L., Dähne, S., Werthen, E., Kappel, E., and Hühne, C.: Equivalent plate formulation of Double–Double laminates for the gradient-based design optimization of composite structures, Composite Structures, 354, 118 786, https://doi.org/https://doi.org/10.1016/j.compstruct.2024.118786, 2025.

Zhao, K., Kennedy, D., Miravete, A., Tsai, S. W., Featherston, C. A., and Liu, X.: Defining the Design Space for Double–Double Laminates by Considering Homogenization Criterion, AIAA Journal, 61, 3190–3203, https://doi.org/10.2514/1.J062639, 2023.